Energy losses and transition radiation in graphene traversed by a fast charged particle under oblique incidence

Kamran Akbari[*]
Department of Applied Mathematics, University of Waterloo, Waterloo, Ontario, Canada N2L 3G1

Silvina Segui[†,‡]
Centro Atómico Bariloche, Comisión Nacional de Energía Atómica, Av. Bustillo 9500, 8400 S.C. de Bariloche, Argentina

Zoran L. Mišković[§]
Department of Applied Mathematics and Waterloo Institute for Nanotechnology, University of Waterloo, Waterloo, Ontario, Canada N2L 3G1

Juana L. Gervasoni[‡] and Néstor R. Arista
Instituto Balseiro, Universidad Nacional de Cuyo and Centro Atómico Bariloche, Comisión Nacional de Energía Atómica, Av. Bustillo 9500, 8400 S.C. de Bariloche, Argentina

(Received 29 August 2018; published 8 November 2018)

We perform fully relativistic calculations of the energy loss channels for a charged particle traversing a single layer of graphene under oblique incidence in a setting pertinent to a scanning transmission electron microscope (STEM), where we distinguish between the energy deposited in graphene in the form of electronic excitations (Ohmic loss) and the energy emitted in the far field in the form of transition radiation (TR). Our formulation of the problem uses a definition of two in-plane, dielectric functions of graphene, which describe the longitudinal and transverse excitation processes that contribute separately to those two energy loss channels. Using several models for the electric conductivity of graphene as the input in those dielectric functions enables us to discuss the effects of oblique incidence on several processes in a broad range of frequencies, from the terahertz (THz) to the ultraviolet (UV). In particular, at the THz frequencies, we demonstrate that the nonlocal effect in the graphene's conductivity is not important in the retarded regime, and we show that the longitudinal and transverse contributions to the emitted TR spectra exhibit strongly anisotropic angular patterns that are readily distinguishable in a cathodoluminescence measurement in a STEM. Moreover, we explore the possibility of exciting the so-called transverse mode in the optical response of graphene at the mid-infrared (MIR) range of frequencies by means of a fast charged particle under oblique incidence. Finally, we demonstrate that, aside from the usual high-energy peaks in the longitudinal contribution to the Ohmic energy loss in the MIR to the UV frequency range, there may arise strongly directional features in the in-plane distribution of the transverse contribution to the Ohmic energy loss for an oblique trajectory, which could be possibly observed via momentum- and angle-resolved electron energy loss spectroscopy of graphene in STEM.

DOI: 10.1103/PhysRevB.98.195410

I. INTRODUCTION

Advances in two-dimensional (2D) materials, coupled with deeper understanding of the physics of their plasmonic features, have opened up a wide range of potential applications [1–4]. Graphene is at the forefront of these developments, both as a reference model for other low-dimensional systems, and for its well-known though intriguing properties [5–8]. Plasmonic applications take advantage from its performance in the terahertz (THz) and mid-infrared (MIR) frequency ranges (0–2 eV), that makes graphene an optimal material for optoelectronic devices, energy storage, biosensing, etc. [7,9–12]. In that range, conveniently doped graphene sustains low-energy plasmon modes that can be tuned using an external gate voltage [13]. But graphene also supports collective excitation modes in the visible to the ultraviolet (UV) range of frequencies (≈2–30 eV), which is dominated by the high-energy interband transitions of π and σ electrons [14].

Electron energy loss spectroscopy (EELS) is a powerful tool used to survey the optical response of materials [15]. Furthermore, EELS implemented in a scanning transmission electron microscope (STEM) has become a reference technique in nanoscience due to its high spatial resolution [16,17], and has been extensively applied to characterize the plasmonic properties of graphene [18–20]. Nowadays, it is possible to obtain momentum-resolved energy loss spectra in the low UV range, including the range 0–2 eV which was usually inaccessible due to the presence of a zero-loss peak [21]. Even spatial mapping of plasmon modes in graphene and

[*]Corresponding author: kakbari@uwaterloo.ca
[†]segui@cab.cnea.gov.ar
[‡]Also at: Consejo Nacional de Investigaciones Científicas y Técnicas of Argentina (CONICET).
[§]zmiskovi@uwaterloo.ca

graphene-related nanostructures has been accomplished in recent works [22,23].

Interaction with external electrons also presents interest for the photonics community, as electron beams impinging on graphene can generate radiation in a range of frequencies from THz to IR and even x ray. Several studies explore this possibility with different electron trajectories including aloof scattering, cyclotron electron beam, and free electron beam [24–26]. Besides, electromagnetic radiation can be measured in a STEM equipped for the detection of cathodoluminescence (CL) light from the target material [27]. This opens the possibility of studying the low-energy losses beyond the detection limit through the emitted radiation patterns. Finally, to further motivate our study here, we mention that the systematic study of radiative and nonradiative losses is known to provide insight into what limits fundamental physical properties of plasmonic systems, for example, plasmon propagation lengths in nanoparticles [28].

In recent papers we have developed a fully relativistic description of the energy losses suffered by an energetic electron perpendicularly traversing a single layer of graphene (SLG) [29], as well as a multilayered graphene stack (MLG) [30,31]. An extension of this work also considered the stopping of electrons traveling on aloof trajectories, parallel to a graphene layer [32]. Our formulation gave analytical expressions for the probability density of energy loss. We have shown that the total energy lost by the electron comes from an Ohmic contribution, due to electronic excitations, and a radiative term due to the so-called transition radiation (TR), generated by the passage of the electron through the interface. The radiative term is purely relativistic and is absent in the parallel trajectory case [32]. For a perpendicular trajectory, only longitudinal fields are relevant since the transverse terms are canceled out due to symmetries of the considered configuration, hence, making it sufficient to consider a scalar in-plane conductivity to describe the response function of graphene [29–31]. For a parallel trajectory, on the other hand, it was found necessary to include transverse polarization in the response of graphene by using a tensorial formulation for its conductivity [32].

In this work, we extend our formalism to an arbitrary oblique trajectory, and accordingly we consider a tensorial conductivity with different components along the longitudinal and the transverse directions with respect to the in-plane wave vector **k**. The formulation is made for a general conductivity tensor, which allows us to apply different models to describe the energy losses of the external charged particle in both the low-energy range (THz to MIR) and in the UV domain. We find that both the longitudinal and transverse excitation mechanisms operate in the case of a general oblique trajectory, which are conveniently described by introducing two in-plane dielectric functions for the response of graphene layer. In each frequency range, we assess contributions to the external particle energy loss coming from both the radiative and nonradiative (Ohmic) channels, and for each one of them we distinguish between the longitudinal and transverse contributions. By exploring the parameter space, specifically, the charged particle speed and its incidence angle, we are able to analyze the ranges of importance for relativistic effects, which govern both the radiative energy loss and the transverse component of the Ohmic energy loss.

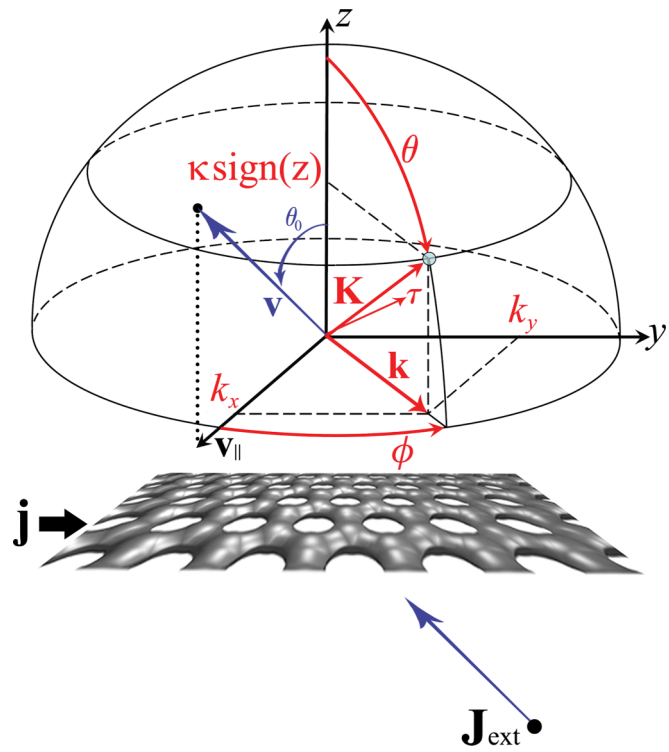

FIG. 1. Geometry of the problem consisting of a 2D graphene sheet placed in vacuum and traversed by a fast charged particle under oblique incidence.

The paper is structured as follows: In Sec. II we describe the theoretical formulation used to obtain the probability densities of energy loss, in terms of the induced electromagnetic fields and the conductivity tensor, giving a detailed description of different models used for the conductivity. Section III is devoted to present and analyze the obtained results. Finally, in Sec. IV we give some concluding remarks. Unless otherwise stated, we use Gaussian units of electrodynamics throughout the paper [33].

II. THEORY

We consider a structure with monolayer graphene of large area placed in the xy plane ($z = 0$) in a three-dimensional (3D) Cartesian coordinate system with coordinates $\mathbf{R} = \{\mathbf{r}, z\}$, where $\mathbf{r} = \{x, y\}$. Graphene is traversed by an external pointlike particle with charge Ze, moving with constant velocity $\mathbf{v}$ at an arbitrary angle θ_0 with respect to the z axis (see Fig. 1). We assume that the structure is placed in vacuum in order to be able to neglect any other sources of radiation or dissipation, apart from those pertaining to graphene. While the assumption of a free-standing graphene layer is realistic in the context of EELS experiments in STEM [18], we note that the existence of a dielectric substrate with the relative dielectric constant $\epsilon_d > 1$ on one side of graphene could possibly give rise to Cherenkov radiation for the incident particle speeds exceeding the threshold $c/\sqrt{\epsilon_d} > 1$, as well as to the transition radiation that normally arises when a

charged particle traverses an interface between materials with different dielectrics constants [33]. Those two sources of radiation would be absent when graphene is surrounded by a homogeneous, nonmagnetic material with the dielectric constant ϵ_d and for the particle speeds below the threshold for Cherenkov radiation, but details of the dispersion relation for the collective modes in graphene would be modified near the THz frequencies by widening of the light cone in such material [34]. At the same time, the magnitude of the incident charged particle electromagnetic (EM) fields would be reduced by a factor of $1/\epsilon_d$, giving rise to an overall reduction of its interaction with the charge carriers in graphene. Moreover, the existence of dynamic modes in the surrounding material(s), which could be encoded via a frequency-dependent dielectric function $\epsilon_d(\omega)$, such as in the case of a polar substrate or nearby metallic gate(s) [35], could give rise to a strong hybridization of their modes with those in graphene [36]. However, studying the above effects of dielectric substrate(s) is beyond the scope of this work.

Considering the geometry of the problem, we find it convenient to introduce a dyadic Green's function (DGF), which may be derived from the electric Hertz vector [37]. This vector can be easily obtained by solving a nonhomogeneous Helmholtz vector equation with an electric current density as the source term by means of a free-space, retarded, scalar Green's function [29].

A. Self-consistent solution for electromagnetic fields

Assuming translational invariance inside the graphene sheet, we may perform a 2D spatial Fourier transform ($\mathbf{r} \to \mathbf{k}$), as well as a Fourier transform with respect to time ($t \to \omega$). Thus, defining the electric field as

$$\mathbf{E}(\mathbf{R}, t) = \iint \frac{d^2\mathbf{k}}{(2\pi)^2} e^{i\mathbf{k}\cdot\mathbf{r}} \int_{-\infty}^{\infty} \frac{d\omega}{2\pi}\, e^{-i\omega t}\mathbf{E}(\mathbf{k}, z, \omega), \quad (1)$$

we may express it in the Fourier space in terms of the corresponding current density $\mathbf{J}$ as

$$\mathbf{E}(\mathbf{k}, z, \omega) = \int_{-\infty}^{+\infty} dz'\, \overleftrightarrow{G}_{e0}(\mathbf{k}, z - z', \omega) \cdot \mathbf{J}(\mathbf{k}, z', \omega), \quad (2)$$

where $\overleftrightarrow{G}_{e0}(\mathbf{k}, z - z', \omega)$ is the electric DGF (EDGF) for free space. Although the above relation can be always expressed in Cartesian coordinates, we take advantage of the fact that graphene is isotropic in the $z = 0$ plane and express all quantities in terms of their longitudinal and transverse (LT) in-plane components. With $\hat{\mathbf{z}}$ being a unit vector in the direction of the z axis, and $\hat{\mathbf{k}}$ the unit vector in the direction of the in-plane wave vector $\mathbf{k}$ that describes longitudinal components, we define the unit vector $\hat{\boldsymbol{\tau}} = \hat{\mathbf{z}} \times \hat{\mathbf{k}}$, which describes transverse in-plane components (see Fig. 1). Thus, adopting the triad $(\hat{\mathbf{k}}, \hat{\boldsymbol{\tau}}, \hat{\mathbf{z}})$, the EDGF may be written in tensorial form as

$$\overleftrightarrow{G}_{e0}(\mathbf{k}, z, \omega) = \frac{i}{\omega}\frac{2\pi}{q}\big\{ -q^2\hat{\mathbf{k}}\hat{\mathbf{k}} + k_0^2\,\hat{\boldsymbol{\tau}}\hat{\boldsymbol{\tau}} - ikq\,\mathrm{sign}(z) \times (\hat{\mathbf{z}}\hat{\mathbf{k}} + \hat{\mathbf{k}}\hat{\mathbf{z}}) + [k^2 - 2q\delta(z)]\,\hat{\mathbf{z}}\hat{\mathbf{z}}\big\} e^{-q|z|}, \quad (3)$$

where $k_0 = \omega/c$ and

$$q(k, \omega) = \begin{cases} -i\frac{\omega}{c}\sqrt{1 - \left(\frac{ck}{\omega}\right)^2} \equiv -i\kappa(k, \omega), & |\omega| > ck \\ \frac{|\omega|}{c}\sqrt{\left(\frac{ck}{\omega}\right)^2 - 1} \equiv \alpha(k, \omega), & |\omega| < ck. \end{cases} \quad (4)$$

In the above equation, $\alpha \equiv \sqrt{k^2 - k_0^2}$ describes the inverse of the localization length for collective excitation modes of charge carriers in graphene that occur in the range of the (k, ω) plane lying outside the light cone.

Defining the volume charge density associated with the external charged particle as $\rho_{\mathrm{ext}}(\mathbf{R}, t) = Ze\delta(\mathbf{R} - \mathbf{v}t)$, we obtain the Fourier transform of the corresponding current density as

$$\mathbf{J}_{\mathrm{ext}}(\mathbf{k}, z, \omega) = \frac{Ze}{v_z}\,\mathbf{v}\, e^{iQz}, \quad (5)$$

where $Q = \Omega/v_z$ with $\Omega = \omega - \mathbf{k}\cdot\mathbf{v}_\parallel$, whereas $\mathbf{v}_\parallel$ and $v_z = \hat{\mathbf{z}}\cdot\mathbf{v} = v\cos\theta_0$, with $v = \|\mathbf{v}\|$, are the parallel and perpendicular components of its velocity $\mathbf{v}$ with respect to the plane of graphene. Given that graphene exhibits in-plane isotropy, it is natural to express wave vector $\mathbf{k}$ using the plane polar coordinates $\mathbf{k} = \{k, \phi\}$, where $k = \|\mathbf{k}\|$ and ϕ is the angle with respect to the direction of $\mathbf{v}_\parallel$, so that $\hat{\mathbf{k}}\cdot\mathbf{v}_\parallel = v_\parallel\cos\phi$ and $\hat{\boldsymbol{\tau}}\cdot\mathbf{v}_\parallel = -v_\parallel\sin\phi$, where $v_\parallel = \|\mathbf{v}_\parallel\| = v\sin\theta_0$. In order to obtain the electric field produced by the external particle, we insert Eqs. (5) and (3) into Eq. (2), giving

$$\mathbf{E}_{\mathrm{ext}}(\mathbf{k}, z, \omega) = \frac{i}{\omega}A(k, \omega)\big[-q^2\hat{\mathbf{k}}\hat{\mathbf{k}} + k_0^2\hat{\boldsymbol{\tau}}\hat{\boldsymbol{\tau}} - kQ(\hat{\mathbf{k}}\hat{\mathbf{z}} + \hat{\mathbf{z}}\hat{\mathbf{k}}) + \left(k_0^2 - Q^2\right)\hat{\mathbf{z}}\hat{\mathbf{z}}\big]\cdot\mathbf{J}_{\mathrm{ext}}(\mathbf{k}, z, \omega), \quad (6)$$

where

$$A(k, \omega) = \frac{4\pi}{q^2 + Q^2}. \quad (7)$$

As a consequence of the dynamic polarization of charge carriers in graphene due to the moving external charge, the induced in-plane charge current in graphene may be expressed via the 2D Ohm's law $\mathbf{j}(\mathbf{k}, \omega) = \overleftrightarrow{\sigma}(k, \omega)\cdot\mathbf{E}_\parallel(\mathbf{k}, 0, \omega)$, where $\mathbf{E}_\parallel(\mathbf{k}, 0, \omega)$ is the component of the total electric field parallel to graphene, evaluated at $z = 0$, simply the in-plane electric field. Here, $\overleftrightarrow{\sigma}(k, \omega)$ is the 2D conductivity tensor of graphene,

$$\overleftrightarrow{\sigma}(k, \omega) = \sigma_l(k, \omega)\hat{\mathbf{k}}\hat{\mathbf{k}} + \sigma_t(k, \omega)\hat{\boldsymbol{\tau}}\hat{\boldsymbol{\tau}}, \quad (8)$$

where any nonlocal effects are expressed via its dependence on $k = \|\mathbf{k}\|$ owing to the isotropy of graphene. Invoking the zero thickness approximation for graphene, the induced current in the structure may be written as

$$\mathbf{J}_{\mathrm{ind}}(\mathbf{k}, z, \omega) = \delta(z)\,\mathbf{j}(\mathbf{k}, \omega) = \delta(z)\,\overleftrightarrow{\sigma}(k, \omega)\cdot\mathbf{E}_\parallel(\mathbf{k}, 0, \omega). \quad (9)$$

We may easily obtain the induced electric field by inserting Eqs. (3) and (9) back into Eq. (2) as

$$\mathbf{E}_{\mathrm{ind}}(\mathbf{k}, z, \omega) = \overleftrightarrow{G}_{e0}(\mathbf{k}, z, \omega)\cdot\overleftrightarrow{\sigma}(k, \omega)\cdot\mathbf{E}_\parallel(\mathbf{k}, 0, \omega). \quad (10)$$

Thus, in order to determine induced electric field throughout the structure, we require a self-consistent procedure to

find the in-plane total electric field $\mathbf{E}_{\parallel}(\mathbf{k}, 0, \omega)$. This may be achieved by taking the in-plane components of Eqs. (5) and (9), followed by setting $z = 0$, and using them to express $\mathbf{E}_{\parallel}(\mathbf{k}, 0, \omega) = \mathbf{E}_{\text{ext}\parallel}(\mathbf{k}, 0, \omega) + \mathbf{E}_{\text{ind}\parallel}(\mathbf{k}, 0, \omega)$. As a result, we obtain a 2D "constitutive relation" in graphene

$$\overleftrightarrow{\epsilon}(\mathbf{k}, \omega) \cdot \mathbf{E}_{\parallel}(\mathbf{k}, 0, \omega) = \mathbf{E}_{\text{ext}\parallel}(\mathbf{k}, 0, \omega), \tag{11}$$

where $\mathbf{E}_{\text{ext}\parallel}(\mathbf{k}, 0, \omega)$ is the component of the external electric field parallel to graphene, evaluated at $z = 0$. In the above equation, we have introduced a 2D dielectric tensor of graphene as

$$\overleftrightarrow{\epsilon}(k, \omega) = \epsilon_l(k, \omega)\hat{\mathbf{k}}\hat{\mathbf{k}} + \epsilon_t(k, \omega)\hat{\boldsymbol{\tau}}\hat{\boldsymbol{\tau}}, \tag{12}$$

where the longitudinal and transverse dielectric functions of graphene are defined as

$$\epsilon_l(k, \omega) = 1 + 2\pi i \frac{q(k, \omega)}{\omega}\sigma_l(k, \omega), \tag{13}$$

$$\epsilon_t(k, \omega) = 1 - 2\pi i \frac{\omega}{c^2 q(k, \omega)}\sigma_t(k, \omega), \tag{14}$$

respectively.

It is clear from Eqs. (11) and (12) that the longitudinal and transverse responses of graphene are decoupled. By evaluating the in-plane external electric field $\mathbf{E}_{\text{ext}\parallel}(\mathbf{k}, 0, \omega)$ from Eq. (6), one can easily solve Eq. (11) for the in-plane total electric field, which we write as $\mathbf{E}_{\parallel}(\mathbf{k}, 0, \omega) = E_{0l}\hat{\mathbf{k}} + E_{0t}\hat{\boldsymbol{\tau}}$, and obtain its longitudinal and transverse components as

$$E_{0l} = \frac{\mathcal{A}}{\epsilon_l}\Big(1 - \frac{\omega}{c^2 k}\hat{\mathbf{k}} \cdot \mathbf{v}_{\parallel}\Big), \tag{15}$$

$$E_{0t} = -\frac{\mathcal{A}}{\epsilon_t}\frac{\omega}{c^2 k}\hat{\boldsymbol{\tau}} \cdot \mathbf{v}_{\parallel}, \tag{16}$$

respectively. Here, $\mathcal{A} = -ik\frac{Ze}{v_z}A$ is the amplitude of the longitudinal component of the in-plane external electric field in the case of normal incidence $\mathbf{v}_{\parallel} = \mathbf{0}$. It is obvious from Eq. (16) that the transverse component of the total in-plane electric field can only be exited in graphene in the case of oblique incidence, i.e., when $\mathbf{v}_{\parallel} \neq \mathbf{0}$.

Finally, having obtained $\mathbf{E}_{\parallel}(\mathbf{k}, 0, \omega) = E_{0l}\hat{\mathbf{k}} + E_{0t}\hat{\boldsymbol{\tau}}$, we can use Eq. (10) to express the induced electric field throughout the structure as

$$\mathbf{E}_{\text{ind}}(\mathbf{k}, z, \omega) = 2\pi e^{-q|z|}\Bigg[\Big(\frac{-iq}{\omega}\sigma_l E_{0l}\Big)\hat{\mathbf{k}} + \Big(\frac{i\omega}{c^2 q}\sigma_t E_{0t}\Big)\hat{\boldsymbol{\tau}} + \Big(\frac{k}{\omega}\,\text{sign}(z)\,\sigma_l E_{0l}\Big)\hat{\mathbf{z}}\Bigg]. \tag{17}$$

Moreover, one can obtain the induced magnetic field by the help of Eq. (17) along with Maxwell's equations as

$$\begin{aligned}\mathbf{H}_{\text{ind}}(\mathbf{k}, z, \omega) &= \frac{1}{ik_0}\Big(i\mathbf{k} + \hat{\mathbf{z}}\frac{\partial}{\partial z}\Big) \times \mathbf{E}_{\text{ind}}(\mathbf{k}, z, \omega) \\ &= \frac{2\pi}{c}e^{-q|z|}\Big[(\sigma_t E_{0t})\,\text{sign}(z)\,\hat{\mathbf{k}} \\ &\quad - (\sigma_l E_{0l})\,\text{sign}(z)\,\hat{\boldsymbol{\tau}} + i\frac{k}{q}(\sigma_t E_{0t})\hat{\mathbf{z}}\Big].\end{aligned} \tag{18}$$

B. Definitions of probability densities

As shown in Refs. [29,30], relativistic treatment of the interaction of an external charged particle with 2D materials in vacuum implies that the total energy lost by that particle goes into two contributions: (1) the Ohmic loss due to the electronic excitations and subsequent damping processes in those materials, and (2) the energy emitted in the far-field region in the form of TR. Accordingly, for each contribution, we may define the corresponding joint probability density as a function of the energy loss $\hbar\omega \geqslant 0$, and the momentum transfer $\hbar\mathbf{k}$, of the external particle. For the total energy loss of the external charged particle, we obtain

$$\begin{aligned}&F_{\text{ext}}(\mathbf{k}, \omega) \\ &= -\frac{1}{4\pi^3\omega}\text{Re}\Big\{\int_{-\infty}^{+\infty} dz\, \mathbf{J}^*_{\text{ext}}(\mathbf{k}, z, \omega) \cdot \mathbf{E}_{\text{ind}}(\mathbf{k}, z, \omega)\Big\} \\ &= \frac{|\mathcal{A}|^2}{4\pi^3\omega}\Bigg[\Big(1 - \frac{\omega}{c^2 k}\hat{\mathbf{k}} \cdot \mathbf{v}_{\parallel}\Big)^2 \text{Re}\Big\{\frac{\sigma_l}{\epsilon_l}\Big\} \\ &\quad + \Big(\frac{\omega}{c^2 k}\hat{\boldsymbol{\tau}} \cdot \mathbf{v}_{\parallel}\Big)^2 \text{Re}\Big\{\frac{\sigma_t}{\epsilon_t}\Big\}\Bigg],\end{aligned} \tag{19}$$

with ϵ_l and ϵ_t given in Eqs. (13) and (14), respectively. The joint density for the Ohmic loss is obtained as

$$\begin{aligned}F_{\text{Ohm}}(\mathbf{k}, \omega) &= \frac{1}{4\pi^3\omega}\text{Re}\Big\{\int_{-\infty}^{+\infty} dz\, \mathbf{J}_{\text{ind}}(\mathbf{k}, z, \omega) \cdot \mathbf{E}^*(\mathbf{k}, z, \omega)\Big\} \\ &= \frac{1}{4\pi^3\omega}\left[|E_{0l}|^2\text{Re}\{\sigma_l\} + |E_{0t}|^2\text{Re}\{\sigma_t\}\right],\end{aligned} \tag{20}$$

with E_{0l} and E_{0t} given in Eqs. (15) and (16), respectively.

The joint density for the radiative energy loss in the upper/lower half-space is obtained from the complex Poynting vector for $\omega > ck$ as

$$F^{\uparrow\downarrow}_{\text{rad}}(\mathbf{k}, \omega) = \frac{1}{4\pi^3\omega}\lim_{z \to \pm\infty}\text{Re}\{\pm\hat{\mathbf{z}} \cdot \boldsymbol{\mathcal{P}}(\mathbf{k}, z, \omega)\}, \tag{21}$$

where the complex Poynting vector is defined via

$$\begin{aligned}\boldsymbol{\mathcal{P}}(\mathbf{k}, z, \omega) &= \frac{c}{4\pi}\mathbf{E}_{\text{ind}}(\mathbf{k}, z, \omega) \times \mathbf{H}^*_{\text{ind}}(\mathbf{k}, z, \omega) \\ &= \frac{\pi}{\omega}\Big(|\sigma_l|^2|E_{0l}|^2 + \frac{\omega^2}{c^2\kappa^2}|\sigma_t|^2|E_{0t}|^2\Big)\mathbf{K},\end{aligned} \tag{22}$$

with $\mathbf{K} = \mathbf{k} + \kappa\,\text{sign}(z)\,\hat{\mathbf{z}}$ being the three-dimensional (3D) wave vector with the magnitude of $\|\mathbf{K}\| = \omega/c$, which represents the direction of the Poynting vector, i.e., the direction of the transfer of EM energy into the far-field region. One may, also, obtain the total radiative energy loss $F_{\text{rad}}(\mathbf{k}, \omega) = F^{\uparrow}_{\text{rad}}(\mathbf{k}, \omega) + F^{\downarrow}_{\text{rad}}(\mathbf{k}, \omega)$ as

$$F_{\text{rad}}(\mathbf{k}, \omega) = \frac{\kappa}{2\pi^2\omega^2}\Bigg[|\sigma_l|^2|E_{0l}|^2 + \Big(\frac{\omega}{c\kappa}\Big)^2|\sigma_t|^2|E_{0t}|^2\Bigg], \tag{23}$$

with E_{0l} and E_{0t} given in Eqs. (15) and (16), respectively. Furthermore, for radiation emitted at a frequency ω in a direction with the angle θ with respect to $\hat{\mathbf{z}}$ and with polar angle ϕ with respect to $\mathbf{v}_{\parallel}$, one can replace $k = \frac{\omega}{c}\sin\theta$ in the expression for $F_{\text{rad}}(\mathbf{k}, \omega) = F_{\text{rad}}(k, \phi, \omega)$ in Eq. (23), and hence obtain the spectral angular distribution of the radiative

energy loss as

$$\mathcal{S}(\theta,\phi,\omega)=\frac{\omega^3}{c^2}|\cos\theta|F_{\rm rad}\left(\frac{\omega}{c}\sin\theta,\phi,\omega\right). \tag{24}$$

It should be mentioned that the longitudinal contribution in Eq. (23) is a result of the term $E_{{\rm ind},l}H^*_{{\rm ind},t}$ in the Poynting vector, so that the radiated wave is TM polarized, whereas the transverse contribution in Eq. (23) is a result of the term $E_{{\rm ind},t}H^*_{{\rm ind},l}$ in the Poynting vector, so that the radiated wave is TE polarized with respect to the direction of propagation $\hat{\mathbf{K}}$ in the far-field region.

One should notice that in all of the above expressions for the joint energy loss densities, Eqs. (19), (20), and (23), the first terms in square brackets represent the contributions of the longitudinal response of graphene, while the second terms in square brackets represent the contributions of the transverse response of graphene. Moreover, it can be easily verified that the conservation of energy is explicitly upheld via the relation $F_{\rm ext}(\mathbf{k},\omega)=F_{\rm Ohm}(\mathbf{k},\omega)+F_{\rm rad}(\mathbf{k},\omega)$. While the radiative losses are restricted to frequencies above the light line, $\omega>ck$, both the total energy loss of the external particle and the Ohmic energy loss occur at all frequencies, $\omega>0$. In a range below the light line, $\omega<ck$, we can denote the energy loss by $F^<_{\rm ext}(\mathbf{k},\omega)=F^<_{\rm Ohm}(\mathbf{k},\omega)$, which may be written in a more familiar form in terms of the longitudinal and transverse loss functions of graphene $\mathrm{Im}\{-1/\epsilon_l\}$ and $\mathrm{Im}\{1/\epsilon_t\}$ as

$$F^<_{\rm Ohm}(\mathbf{k},\omega)=\frac{2}{\pi^2}\left(\frac{Ze}{v_z}\right)^2\frac{1}{(\alpha^2+Q^2)^2\alpha}\Bigg[(k-k_0\beta_\parallel\cos\phi)^2\times\mathrm{Im}\left\{\frac{-1}{\epsilon_l}\right\}+\alpha^2\beta_\parallel^2\sin^2\phi\,\mathrm{Im}\left\{\frac{1}{\epsilon_t}\right\}\Bigg], \tag{25}$$

where we have defined the reduced parallel speed as $\beta_\parallel=v_\parallel/c$. In the nonretarded limit, one should set $\beta_\parallel\to0$ and change $\alpha\to k$ in Eq. (25), confirming that transverse response of graphene only arises in a fully retarded regime.

It is further of interest to study the role of collective modes pertaining to the charge carrier excitations in graphene. Those modes can be formally identified in domains of the (k,ω) plane where (a) the interband electron transitions may be neglected, (b) Landau damping due to the continuum of electron-hole excitations is absent, and (c) dissipative processes due to electron scattering on impurities, phonons, or atomic-scale defects in graphene are sufficiently small. Under such conditions, one may set $\mathrm{Re}\{\sigma_l\}\to0^+$ and $\mathrm{Re}\{\sigma_t\}\to0^+$, so that the loss functions $\mathrm{Im}\{-1/\epsilon_l\}$ and $\mathrm{Im}\{1/\epsilon_t\}$ in Eq. (25) become proportional to Dirac delta functions peaked along the dispersion relations for longitudinal and transverse modes in graphene $\omega=\omega_l(k)$ and $\omega=\omega_t(k)$, respectively. The corresponding eigenfrequencies $\omega_l(k)$ and $\omega_t(k)$ may be obtained under such conditions by solving the equations $\mathrm{Re}\{\epsilon_l(k,\omega)\}=0$ and $\mathrm{Re}\{\epsilon_t(k,\omega)\}=0$, where

$$\mathrm{Re}\{\epsilon_l(k,\omega)\}=1-2\pi\frac{\alpha(k,\omega)}{\omega}\mathrm{Im}\{\sigma_l(k,\omega)\}, \tag{26}$$

$$\mathrm{Re}\{\epsilon_t(k,\omega)\}=1+2\pi\frac{\omega}{c^2\alpha(k,\omega)}\mathrm{Im}\{\sigma_t(k,\omega)\}, \tag{27}$$

showing that the longitudinal and transverse modes in graphene can only exist at frequencies below the light line, such that $\mathrm{Im}\{\sigma_l(k,\omega)\}>0$ and $\mathrm{Im}\{\sigma_t(k,\omega)\}<0$, respectively.

Finally, an integrated probability density can be expressed as the integration of the joint probability densities over the whole wave-vector range via

$$P_\Lambda(\omega)=\frac{1}{\hbar^2}\iint d^2\mathbf{k}\,F_\Lambda(\mathbf{k},\omega)=\frac{1}{\hbar^2}\int_0^{2\pi}d\phi\int_0^\infty dk\,k\,F_\Lambda(k,\phi,\omega), \tag{28}$$

where $\Lambda=$ ext, Ohm, rad. As one would expect, the energy conservation maintains that $P_{\rm ext}(\omega)=P_{\rm Ohm}(\omega)+P_{\rm rad}(\omega)$ for all $\omega>0$.

C. Models of conductivity

For the optical response of graphene in the THz-MIR range of frequencies, it suffices to take into account low-energy excitations involving its π electron bands described within the Dirac cone approximation. We consider in this work three models of conductivity of doped graphene in this range of frequencies: (a) Drude model for intraband excitations, suitable at THz frequencies, (b) optical conductivity of graphene combining the intraband and interband excitations, suitable at the THz to MIR frequencies, and (c) a model due to Lovat *et al.* [38], which includes the intraband electron-hole continuum of excitations, and is suitable at THz frequencies and finite wave numbers k. While the Drude model and the optical conductivity are given in a strict long-wavelength limit $k\to0$, the Lovat's model introduces nonlocal effects into the Drude model.

We note that the longitudinal and transverse conductivities of graphene, $\sigma_l(k,\omega)$ and $\sigma_t(k,\omega)$, are generally different quantities when the wave number k is finite, as in the case of Lovat's model, but in the long-wavelength limit, they both become equal to a frequency-dependent conductivity of graphene, $\sigma_l(0,\omega)=\sigma_t(0,\omega)=\sigma(\omega)$, which may be modeled either by the Drude conductivity or by the optical conductivity of graphene.

We will also consider a higher-frequency range, corresponding to the energy losses of $\omega\gtrsim1$ eV, which is usually probed in the low-energy EEL spectrum obtained with a (S)TEM [18,19,39,40]. In this case, we employ a two-fluid hydrodynamic model (HD) suitable for describing high-energy interband electron transitions in intrinsic (undoped) graphene in the optical regime, which we amend by a Dirac correction to account for the lower-energy interval [41].

1. Drude model conductivity

It has been shown that the intraband excitations in doped graphene are well represented by a Drude-type model of conductivity [42,43], which is given at finite temperature T by

$$\sigma_{\rm intra}(\omega)=\frac{i}{4\pi}\frac{v_F^2k_{\rm TF}}{\omega+i\gamma}, \tag{29}$$

where $k_{\rm TF}=8e^2\frac{k_BT}{(\hbar v_F)^2}\ln\left[2\cosh\left(\frac{\mu}{2k_BT}\right)\right]$ is the Thomas-Fermi wave number, with μ being the chemical potential of graphene and $v_F\approx c/300$ its Fermi speed. In the zero-

temperature limit, one obtains $\mu \to \mathcal{E}_F = \hbar v_F k_F$ and hence $k_{\rm TF} \to 4\frac{v_B}{v_F}k_F$, where $\mathcal{E}_F$ is the Fermi energy of graphene and $k_F = \sqrt{\pi|n|}$ its Fermi wave number for charge carrier density n, whereas $v_B \equiv \frac{e^2}{\hbar} \approx c/137$ is the Bohr speed. In Eq. (29), γ is the damping rate due to electron scattering processes, which is largely unknown parameter that depends on the purity of graphene.

It is convenient to adopt nondimensionalized variables $\overline{k} = \frac{k}{k_c}$ and $\overline{\omega} = \frac{\omega}{\omega_c}$, where $k_c = \frac{1}{4}k_{\rm TF}(\frac{v_F}{c})^2$ and $\omega_c = ck_c$. We note that, for typical doping densities of graphene, the relevant unit of frequency is $\nu_c = \frac{2\pi}{\omega_c} \sim 1$ THz. Thus, the Drude conductivity is given in reduced form by $\overline{\sigma}_{\rm intra} \equiv \frac{\sigma_{\rm intra}}{c} = \frac{i}{\pi}\frac{1}{\overline{\omega}+i\overline{\gamma}}$, where $\overline{\gamma} = \frac{\gamma}{\omega_c}$ is the reduced damping rate. In an idealized case when $\overline{\gamma} \to 0$, upon using the Drude conductivity in Eqs. (26) and (27), one obtains a longitudinal mode pertaining to the so-called Dirac plasmon polariton (DPP), whereas no transverse modes exist because $\mathrm{Im}\{\overline{\sigma}_{\rm intra}\} > 0$. A dispersion relation for the DPP mode obtained from the Drude model may be then expressed in a simple form using the reduced variables as $\overline{\alpha} = \frac{1}{2}\overline{\omega}^2$, where $\overline{\alpha} \equiv \frac{\alpha}{k_c} = \sqrt{\overline{k}^2 - \overline{\omega}^2}$.

The range of validity of the Drude model in Eq. (29) is given by a double inequality $kv_F \ll \omega \ll \omega_F$, where $\omega_F = \mathcal{E}_F/\hbar$ is the frequency associated with the Fermi energy in graphene [44]. In the reduced units, these inequalities amount to $\frac{v_F}{c}\overline{k} \ll \overline{\omega} \ll \varphi$, where $\varphi \equiv \frac{c}{v_B} \approx 137$ is the inverse of the fine structure constant.

2. Nonlocal model conductivity

Effects due to finite wave number k can be introduced into the conductivity of graphene at sufficiently low frequencies, such that $\omega \ll \omega_F$, by using the model developed by Lovat *et al.* [38]. Their model essentially generalizes the Drude conductivity by introducing the effects of intraband electron-hole continuum in the domain $0 < \omega < kv_F$ of the (k, ω) plane, thereby relaxing the lower-frequency constraint of the Drude model $kv_F \ll \omega$. Those authors obtained the longitudinal and transverse conductivities of graphene, which may be expressed in the reduced units used in our work as

$$\overline{\sigma}_l(\overline{k}, \overline{\omega}) = 2\,\frac{\overline{\sigma}_{\rm intra}}{1+\chi}\,\frac{1}{\chi - i\frac{\overline{\gamma}}{\overline{\omega}}(1-\chi)}, \tag{30}$$

$$\overline{\sigma}_t(\overline{k}, \overline{\omega}) = 2\,\frac{\overline{\sigma}_{\rm intra}}{1+\chi}, \tag{31}$$

respectively. Here, $\overline{\sigma}_{\rm intra}(\overline{\omega})$ is the Drude conductivity given in Eq. (29) and the auxiliary factor $\chi(\overline{k}, \overline{\omega})$ is defined as

$$\chi = \sqrt{1 - \left(\frac{v_F}{c}\right)^2\left(\frac{\overline{k}}{\overline{\omega}+i\overline{\gamma}}\right)^2}. \tag{32}$$

While the longitudinal and transverse conductivities attain different values in the model due to Lovat *et al.*, the smallness of the factor $(\frac{v_F}{c})^2 \approx 10^{-5}$ indicates that nonlocal effects are only observable at frequencies $\overline{\omega} \ll \overline{k}$, which lie deeply in the nonretarded regime, and hence they are expected to be suppressed in the transverse response of graphene in comparison to its longitudinal response. Therefore, to the order of $(\frac{v_F}{c})^2 \approx 10^{-5}$, the longitudinal and transverse conductivities become equal, and are given by the Drude model $\overline{\sigma}_l = \overline{\sigma}_t = \overline{\sigma}_{\rm intra}(\overline{\omega})$.

On the other hand, taking the limit $\overline{\gamma} \to 0$ for frequencies outside the continuum of intraband single-electron excitations $\overline{\omega} > \overline{k}\,\frac{v_F}{c}$, one can ensure that the real parts of both $\overline{\sigma}_l$ and $\overline{\sigma}_t$ vanish, while their imaginary parts are found to be both positive. Therefore, by using Eqs. (30) and (31) in Eqs. (26) and (27), respectively, it follows that only a longitudinal mode exists with a dispersion relation, which is very close to that of a DPP mode from the Drude conductivity model.

3. Optical model conductivity

The upper frequency constraint of the Drude model $\omega \ll \omega_F$ may be relaxed by adding to it the low-energy interband contribution, which is sometimes called Dirac conductivity. This contribution is given at zero temperature by [42,45]

$$\sigma_{\rm inter}(\omega) = i\frac{v_B}{4\pi}\ln\left(\frac{2\omega_F - \omega - i\gamma}{2\omega_F + \omega + i\gamma}\right). \tag{33}$$

It was shown by *ab initio* calculations [36] that, in the strict long-wavelength limit, the conductivity of graphene at frequencies up to about $2\omega_F$ is well represented by the sum of the intraband and interband contributions given in Eqs. (29) and (33), $\sigma_{\rm opt}(\omega) = \sigma_{\rm intra}(\omega) + \sigma_{\rm inter}(\omega)$, respectively. We shall call such model optical conductivity and apply it to the range of frequencies up to MIR, corresponding to an energy loss of the incident particle of about 1 eV.

Switching to reduced variables, we note that in the zero damping limit $\overline{\gamma} \to 0$, the reduced interband conductivity becomes [45]

$$\overline{\sigma}_{\rm inter} = \frac{1}{4\varphi}\left[\Theta(\overline{\omega} - 2\varphi) + \frac{i}{\pi}\ln\left|\frac{\overline{\omega} - 2\varphi}{\overline{\omega} + 2\varphi}\right|\right], \tag{34}$$

where Θ is the unit step function. One observes that $\mathrm{Re}\{\overline{\sigma}_{\rm inter}\} \approx 0$ and $\mathrm{Im}\{\overline{\sigma}_{\rm inter}\} < 0$ for frequencies $\overline{\omega} < 2\varphi \approx 274$, thus opening the possibility for excitation of a transverse mode in that interval. Indeed, by taking $\overline{\gamma} \to 0$ in that same frequency interval for the optical conductivity, we ensure that its real part vanishes $\mathrm{Re}\{\overline{\sigma}_{\rm opt}(\overline{\omega})\} \to 0$, while its imaginary part $\mathrm{Im}\{\overline{\sigma}_{\rm opt}(\overline{\omega})\}$ changes its sign at a critical frequency $\overline{\omega}_* \approx 1.667\,\varphi \approx 228$. Therefore, using the optical conductivity $\overline{\sigma}_{\rm opt}(\overline{\omega})$ in Eqs. (26) and (27), one finds that a longitudinal mode can be excited at frequencies $0 < \overline{\omega} < \overline{\omega}_*$ and a transverse mode can be excited in the interval $\overline{\omega}_* < \overline{\omega} < 2\varphi$. We note that this interval covers a range around 1 eV, using the physical units. The corresponding dispersion relations of those modes are given in reduced units as $\overline{\alpha} = \overline{\alpha}_l(\overline{\omega})$ and $\overline{\alpha} = \overline{\alpha}_t(\overline{\omega})$, where

$$\overline{\alpha}_l(\overline{\omega}) = \frac{\overline{\omega}^2}{2}\left[1 + \frac{\overline{\omega}}{4\varphi}\ln\left(\frac{2\varphi - \overline{\omega}}{2\varphi + \overline{\omega}}\right)\right]^{-1}, \quad 0 < \overline{\omega} < \overline{\omega}_* \tag{35}$$

$$\overline{\alpha}_t(\overline{\omega}) = -2\left[1 + \frac{\overline{\omega}}{4\varphi}\ln\left(\frac{2\varphi - \overline{\omega}}{2\varphi + \overline{\omega}}\right)\right], \quad \overline{\omega}_* < \overline{\omega} < 2\varphi. \tag{36}$$

Therefore, in the case of optical conductivity, we can use Eq. (25) to obtain a modal decomposition in the regime when $\mathrm{Re}\{\overline{\sigma}(\overline{\omega})\} \to 0$, where the loss functions for the longitudinal and transverse responses of graphene are to be replaced by the

Dirac delta functions, according to

$$\mathrm{Im}\left\{\frac{-1}{\epsilon_l}\right\} \to \pi\overline{\alpha}_l(\overline{\omega})\,\delta(\overline{\alpha}-\overline{\alpha}_l(\overline{\omega})) \quad \text{for} \quad 0<\overline{\omega}<\overline{\omega}_*, \tag{37}$$

$$\mathrm{Im}\left\{\frac{1}{\epsilon_t}\right\} \to \pi\overline{\alpha}_t(\overline{\omega})\,\delta(\overline{\alpha}-\overline{\alpha}_t(\overline{\omega})) \quad \text{for} \quad \overline{\omega}_*<\overline{\omega}<2\varphi, \tag{38}$$

respectively.

We note that the transverse mode in doped graphene was predicted by Mikhailov and Ziegler [46], and was studied in some detail by Stauber [47], but its confirmation has eluded experimentalists so far. Therefore, we use the optical model of conductivity to explore here the possibility to excite the transverse mode in graphene via electron beam under oblique incidence.

It is interesting to mention that, if a small gap Δ is opened between graphene's valence and conduction π electron bands, then the optical conductivity for an undoped graphene would be given by an expression similar to that given in Eq. (33) for interband transitions, but with the frequency ω_F replaced by $\Delta/(2\hbar)$ [47]. When a graphene layer that exhibits a finite gap Δ is also doped with its Fermi level shifted into the conduction or the valence band, then its optical conductivity would consist of both interband term governed by Δ and an intraband term of the Drude form in Eq. (29), governed by the doping density of gapped graphene.

4. Extended hydrodynamic model conductivity

The optical response of graphene in the range of high frequencies, from MIR to UV, corresponding to the energy losses in an interval 1–30 eV, is characterized by the high-energy $\pi \to \pi^*$ and $\sigma \to \sigma^*$ interband transitions [48,49]. The energy loss function shows conspicuous features at about 4 and 14 eV [50,51], which are usually labeled as the π and $\sigma+\pi$ "plasmon" peaks, and their dispersion can be assessed through standard k-resolved EELS experiments [40]. In that range of energies, a two-fluid hydrodynamic (HD) model was found to be a good description for the polarization function χ_0, obtained as the sum of the contributions from π and σ electrons, $\chi_0 = \chi_\pi + \chi_\sigma$, with

$$\chi_\nu(q,\omega) = \frac{n_\nu^0 q^2/m_\nu^*}{s_\nu^2 q^2 + \omega_{\nu r}^2 - \omega(\omega + i\gamma_\nu)}, \tag{39}$$

where n_ν^0, m_ν^*, $\omega_{\nu r}$, $s_{\nu r}$, and γ_ν are the equilibrium surface number density of electrons, effective electron mass, restoring frequency, acoustic speed, and the damping rate in the νth fluid (where $\nu = \pi, \sigma$), respectively. In the optical limit, the conductivity of graphene is obtained as the sum of two Drude-Lorentz–type terms

$$\begin{aligned}\sigma_{\mathrm{HD}}(\omega) &= -ie^2\omega \lim_{q\to 0}\frac{\chi_0(q,\omega)}{q^2} \\ &= -ie^2\omega\left[\frac{n_\pi^0/m_\pi^*}{\omega_{\pi r}^2 - \omega(\omega+i\gamma_\pi)} + \frac{n_\sigma^0/m_\sigma^*}{\omega_{\sigma r}^2 - \omega(\omega+i\gamma_\sigma)}\right].\end{aligned} \tag{40}$$

While this model provided a good fit of the dominant π and $\sigma+\pi$ peak structures in the spectra of graphene at energy losses $\gtrsim$3 eV [18,51], there are indications in the more recent experimental data that the Dirac physics of low-energy excitations in graphene could play an important role at energy losses $\lesssim$2 eV [19,21,39,41]. The inadequacy of the model in Eq. (40) at such energies is readily indicated by the fact that $\sigma_{\mathrm{HD}}(0) = 0$, whereas the conductivity of undoped graphene should approach the value of $v_B/4$ when $\omega \to 0$, i.e., the so-called universal optical conductivity of graphene [52]. In order to include the low-energy range, Djordjević *et al.* [41] extended the hydrodynamic model by adding a Dirac term $\sigma_D(\omega)$ describing the $\pi \to \pi^*$ interband electron transitions that occur near the K points in the Brillouin zone of graphene. The structure of the extended HD (eHD) model and its various parameters are determined through the application of the Kramers-Kronig relations and the f-sum rule, which maintains the conservation of the number of electrons participating in various excitation processes [41]. This yields the conductivity of undoped graphene in the form

$$\begin{aligned}\sigma_{\mathrm{eHD}}(\omega) = e^2\Bigg\{&\frac{1}{4\hbar}\frac{\omega_*^4}{\omega_*^4+\omega^4} + i\frac{\omega}{m_e}\Bigg[\frac{\omega_*^2+\omega^2}{\omega_*^4+\omega^4}\frac{\omega_* m_e\sqrt{2}}{8\hbar} \\ &- \left(1 - \frac{\omega_* m_e\sqrt{2}}{8\hbar n_{at}}\right)\frac{n_\pi^0}{\omega_{\pi r}^2 - \omega(\omega+i\gamma_\pi)} \\ &- \frac{n_\sigma^0}{\omega_{\sigma r}^2 - \omega(\omega+i\gamma_\sigma)}\Bigg]\Bigg\}.\end{aligned} \tag{41}$$

It should be noted that the addition of the Dirac term introduces a parameter ω_* in Eq. (41), so that the universal conductivity of graphene is approached when $\omega \ll \omega_*$, giving $\sigma_{\mathrm{eHD}}(0) = v_B/4$. The parameter ω_* may be qualitatively interpreted as a cutoff frequency that separates the low-energy $\pi \to \pi^*$ electron transitions near the K points in the Brillouin zone of undoped graphene, which give rise to the universal conductivity when $\omega \to 0$, from the high-energy $\pi \to \pi^*$ electron transitions near the M points, which give rise to the π plasmon peak near $\omega_{\pi r}$ [41].

We adopt the above model with the following values for the parameters: $n_\pi^0 = n_{at} = 38\ \mathrm{nm}^{-2}$, $n_\sigma^0 = 114\ \mathrm{nm}^{-2}$, $\omega_{\pi r} = 4.19$ eV, $\omega_{\sigma r} = 14.15$ eV, $\gamma_\pi = 2.04$ eV, $\gamma_\sigma = 2.178$ eV, and $\omega_* = 3.54$ eV. These values ensure that the model reproduces satisfactorily several sets of experimental data for EELS on single-layered graphene [41], and agrees well with *ab initio* calculations of graphene's optical conductivity in a broad range of frequencies [36].

III. RESULTS AND DISCUSSION

In this section, we present calculations corresponding to the energy loss spectra of the electrons impinging on graphene under oblique incidence, using the conductivity models described in the previous section for diverse frequency regimes. One should note that, while the results of calculations using the eHD conductivity model for the high-frequency range are presented in the physical units, it is convenient to nondimensionalize the relevant variables in the other three models for low frequencies, covering the THz to MIR range, as described in the previous section.

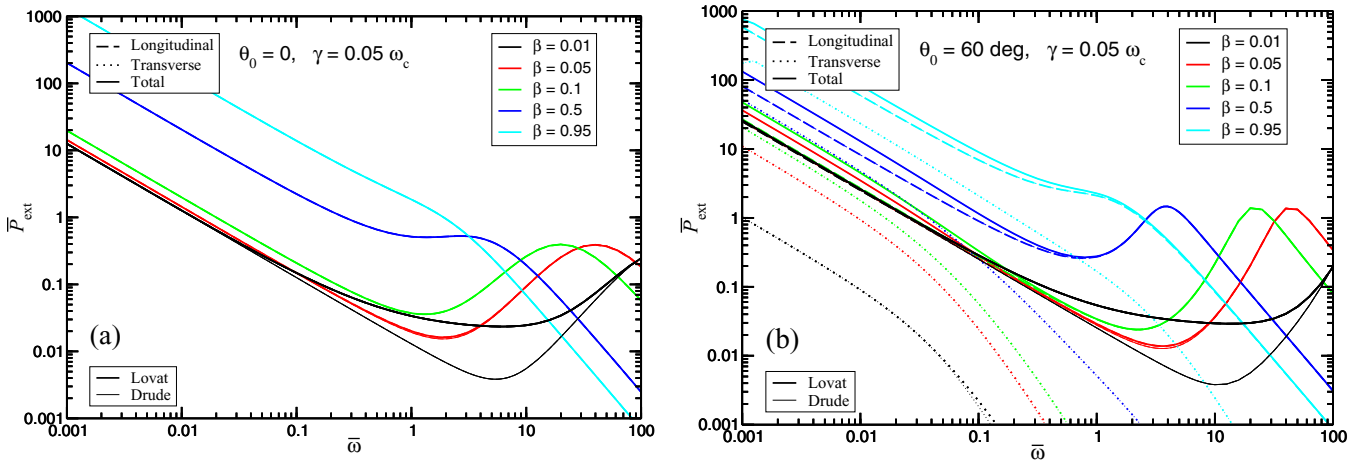

FIG. 2. Normalized integrated energy loss density of the external charged particle $\overline{P}_{\rm ext} = P_{\rm ext}/P_c$ with $P_c = 4/(\pi\mathcal{E}_F)$ where $\mathcal{E}_F$ is the Fermi energy of graphene, for two angles of incidence: (a) $\theta_0 = 0$ and (b) $\theta_0 = 60^\circ$, and for several external particle speeds β, versus the reduced frequency $\overline{\omega} = \omega/\omega_c$. Also shown are, in each panel, two separate contributions of longitudinal (dashed curves) and transverse (dotted curves) dielectric functions to the external loss. Nonlocal effects of the graphene's conductivity model on the loss spectra is depicted by the comparison of the Lovat's (thick lines) and Drude (thin lines) models. The reduced damping rate is fixed at $\overline{\gamma} = \gamma/\omega_c = 0.05$.

There are several parameters that influence the low-energy loss spectra; two of them are associated with the external charged particle, i.e., the direction of its motion relative to graphene (quantified by θ_0) and its speed (quantified by β), and two of them are associated with the graphene sheet, i.e., the damping of its charge carriers' excitations (quantified by the rate γ) and the collective excitations of its charge carriers, or plasmon polariton modes described by the corresponding dispersion relations in the (k, ω) plane. In the low-frequency regime, we shall keep the normalized damping ratio fixed at a relatively low value of $\overline{\gamma} = 0.05$, unless we turn to a discussion of the role of the dispersion relations, which are obtained from the zeros of the dielectric functions in Eqs. (13) and (14) in the limit of vanishing damping. We have chosen a relatively small value of $\overline{\gamma} = 0.05$ in order to emphasize resonant features in the spectra due to the excitation of plasmon polariton modes at low-energy losses. However, it should be stressed that we have found in our previous publications that increasing values of $\overline{\gamma}$ exert rather strong influence on both the Ohmic and radiation energy losses, especially at the sub-THz frequencies [29–31].

Throughout this section, we shall present and compare the decomposition of all energy-loss channels into their longitudinal and transverse components in order to emphasize the importance of the oblique trajectories of the external particle for generating EM fields with different polarizations by the two types of the excitation mechanisms of charge carriers in graphene, which are descried by the dielectric functions in Eqs. (13) and (14).

A. Energy losses at the THz frequencies

The dynamic response of graphene in the THz range of frequencies is expected to be well described by the Lovat's model, as well as by the Drude model as its local limit. By comparing the results from those two models, we can directly assess the effects of nonlocality in the energy loss densities at those frequencies.

Figure 2 shows the normalized integrated energy loss density of the external charged particle $\overline{P}_{\rm ext} = P_{\rm ext}/P_c$ with $P_c = 4/(\pi\mathcal{E}_F)$ where $\mathcal{E}_F$ is the Fermi energy of graphene, for two angles of incidence: $\theta_0 = 0$ in Fig. 2(a) and $\theta_0 = 60^\circ$ in Fig. 2(b), and for several external particle speeds β. We also show in each panel two separate contributions to the function $\overline{P}_{\rm ext}(\overline{\omega})$ coming from the longitudinal (dashed curves) and transverse (dotted curves) dielectric functions [see Eq. (19) with Eq. (28)].

Under the normal incidence ($\theta_0 = 0$), shown in Fig. 2(a), there only exists a longitudinal contribution to the energy loss density $\overline{P}_{\rm ext}(\overline{\omega})$. The effect of nonlocality only becomes visible in the frequency range $0.1 \lesssim \overline{\omega} \lesssim 100$ for the very low speed of $\beta = 0.01$, i.e., in the nonretarded regime. For the low-frequency range $\overline{\omega} \lesssim 0.1$, the function $\overline{P}_{\rm ext}(\overline{\omega})$ exhibits a $\propto\overline{\omega}^{-1}$ dependence and increases in magnitude with the increasing speed of the charged particle. This is consistent with the findings of our previous work [29,31], where it was shown that both the Ohmic energy loss (for finite damping rate) and the radiative energy loss exhibit the characteristic $\propto\overline{\omega}^{-1}$ dependence when $\overline{\omega} \to 0^+$, with their respective magnitudes increasing with β. Specifically, for the Ohmic energy loss, this can be seen from Eq. (15) in Ref. [31], whereas for the radiative energy loss, one can obtain from Eq. (48) in Ref. [29] that, in the limit $\overline{\omega} \to 0^+$ and for zero damping, the normalized integrated radiation energy loss density scales as $\overline{P}_{\rm rad}(\overline{\omega}) \sim \frac{2}{3}\frac{\beta^2}{\overline{\omega}}$ to within an accuracy of 10% for the normal incidence at the speeds $\beta \lesssim 0.5$.

On the other hand, a peak is observed in Fig. 2(a) at frequencies $\overline{\omega} \gtrsim 1$, where the Ohmic energy loss plays a dominant role (see Fig. 3 in Ref. [29]). That peak results from an interplay of the longitudinal Dirac plasmon polariton (LDPP) mode in graphene and the amplitude $|\mathcal{A}|^2$ [see Eq. (19)]. The position of this LDPP-induced peak is seen in Fig. 2(a) to shift towards higher frequencies as the particle speed decreases. To understand such behavior of the peak in the energy loss spectra under the normal incidence, it suffices to consider the limit of zero damping, and refer to Eq. (47) in Ref. [29], which

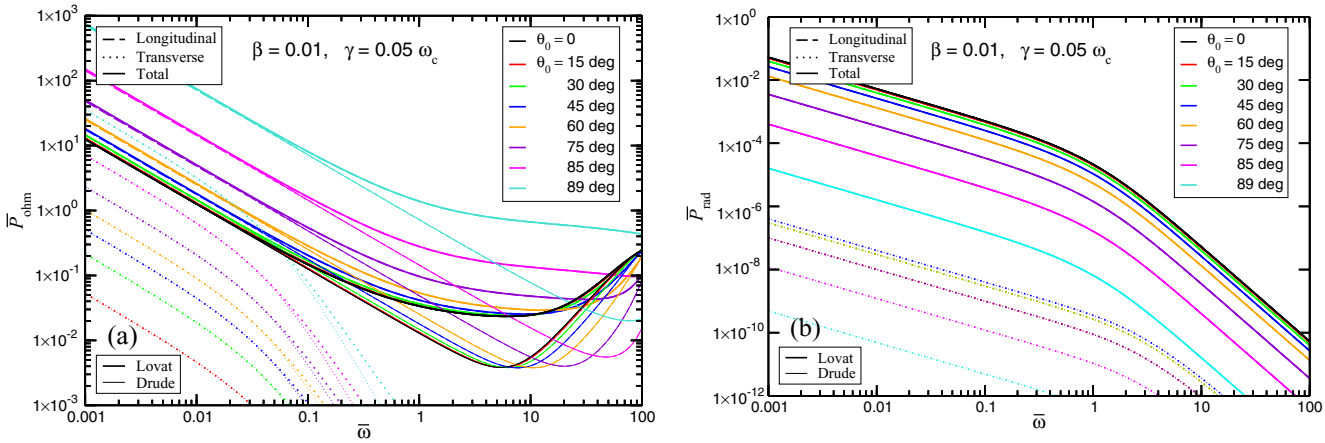

FIG. 3. Normalized integrated probability densities for (a) Ohmic energy loss $\overline{P}_{\rm Ohm}(\overline{\omega}) = P_{\rm Ohm}/P_c$ and (b) radiative energy loss $\overline{P}_{\rm rad}(\overline{\omega}) = P_{\rm rad}/P_c$ for the charged particle speed of $\beta = 0.01$ (the nonretarded case) and for several angles of incidence. The differences between the Lovat's (thick lines) and Drude (thin lines) models, as well as the relative weights of the longitudinal (dashed lines) and transverse (dotted lines) contributions to the Ohmic and radiative integrated densities in a nonretarded limit, are also shown. The reduced damping rate is fixed at $\overline{\gamma} = 0.05$.

yields a peak in the integrated Ohmic energy loss density that is positioned at $\overline{\omega}_{\rm peak} = 2\sqrt{\beta^{-2} - 2}$. This shows that the peak frequency decreases with increasing speed, and the peak disappears for the speeds $\beta > 1/\sqrt{2}$.

When the charged particle's trajectory becomes oblique to the plane of graphene, the transverse part begins to contribute to the energy loss density $\overline{P}_{\rm ext}(\overline{\omega})$, which is shown in Fig. 2(b) with the same speeds as in Fig. 2(a), but for the angle of incidence of $\theta_0 = 60^\circ$ [53]. It is observed that the transverse part mostly contributes to the energy loss in the low-frequency range. Even though the transverse contribution remains generally smaller than the longitudinal contribution, their magnitudes can become comparable, e.g., for the speed $\beta \sim 0.1$ at frequencies $\overline{\omega} \lesssim 0.01$, as seen in Fig. 2(b). Furthermore, the effect of the nonlocality, which is exposed by comparing the Lovat's and Drude models for both the longitudinal and transverse contributions, appears to be similar to what was observed in Fig. 2(a). Namely, the nonlocal effect is only visible for sufficiently low speeds, i.e., in the nonretarded regime and, while it affects the longitudinal contribution in the same range of frequencies as in the case of the normal incidence, the nonlocal effect is practically ignorable for the transverse contribution, as indicated by the dotted black lines in Fig. 2(b). It is further noticed that both the transverse and the longitudinal contributions exhibit the same characteristic $\propto \overline{\omega}^{-1}$ dependence at the lowest frequencies, which is accompanied by an increase in magnitude with increasing particle speed, similar to the behavior observed in Fig. 2(a). On the other hand, while the longitudinal contribution exhibits a LDPP-induced peak at frequencies $\overline{\omega} \gtrsim 1$ in Fig. 2(b), with a similar peak position as in Fig. 2(a), the transverse contribution is heavily suppressed at such frequencies.

As was noticed above, the nonlocal effects only matter at low speeds, i.e., in the nonretarded regime. In order to investigate this regime in some detail, we study in Fig. 3 the normalized integrated densities for both the Ohmic energy loss $\overline{P}_{\rm Ohm} = P_{\rm Ohm}/P_c$, in Fig. 3(a), and the radiative energy loss $\overline{P}_{\rm rad} = P_{\rm rad}/P_c$, in Fig. 3(b), for the charged particle speed of $\beta = 0.01$ and for several angles of incidence. In this figure, one can further clarify the differences between the Lovat's and Drude models, as well as elucidate the relative weights of the longitudinal and transverse contributions to the Ohmic and radiative integrated densities in a nonretarded limit. As expected for this low speed, the effect of nonlocality is apparent at frequencies $\overline{\omega} \gtrsim 0.1$, but only for the Ohmic energy loss, as shown in Fig. 3(a). At the same time, Fig. 3(b) confirms that there is no effect of the nonlocality in the radiative energy loss, neither in the longitudinal nor in the transverse contributions, which is expected since the radiation loss is a purely relativistic phenomenon.

Regarding the magnitude of various contributions to the energy loss in Fig. 3, one notices that the radiative loss channels are significantly smaller than the corresponding Ohmic loss channels, as expected at such low speed. Moreover, the nonretarded regime is also responsible for the transverse contributions to both the Ohmic and the radiative energy losses being much smaller than the corresponding longitudinal contributions. Comparing Figs. 3(a) and 3(b) in that figure at frequencies $\overline{\omega} \lesssim 1$, one further notices that the longitudinal contribution to the Ohmic energy loss increases, while the same contribution to the radiation energy loss decreases with increasing angle of incidence θ_0. The latter observation is consistent with the observations in Fig. 2, implying that it is the normal component of the external particle speed $\beta \cos\theta_0$ that likely governs the magnitude of the longitudinal contribution to the radiative energy loss channels. Namely, given that the radiation is most effectively produced by accelerating the charge carriers in graphene, a reduction in the perpendicular component of the speed would bring down the "abruptness" of graphene's interaction with the external charged particle and hence reduce the production of TR. Clearly, for a strictly parallel trajectory, there can be no radiation [32]. For a more quantitative assessment, one may invoke the analysis of Fig. 2(a) based on Eq. (48) in Ref. [29], and hence surmise that the longitudinal contribution to the radiative energy loss scales as $\propto(\beta\cos\theta_0)^2$.

Regarding the dependence of the transverse contributions to the Ohmic and radiative energy losses on the incident angle, similar conclusions can be drawn as for the longitudinal contributions, with a peculiar "anomaly" seen in Fig. 3(b), where the transverse contribution to the radiative energy loss exhibits an apparently symmetric maximum about the incident angle $\theta_0 = \pi/4$. This can be explained in the following way. By looking at the transverse part of Eq. (23), with the transverse component of the in-plane tangential electric field given in Eq. (16), which contains the factor $\hat{\boldsymbol{\tau}} \cdot \mathbf{v}_\parallel$. Therefore, the magnitude of the transverse contribution to the radiative energy loss is proportional to $\sin^2\theta_0$, so it vanishes as the incident particle approaches graphene under a grazing angle of incidence, i.e., on a near-parallel trajectory. On the other hand, one notices in Fig. 3(b) that there exist equal spacings between any pair of the curves representing the transverse or longitudinal contributions to the radiative energy loss at low frequencies, $\overline{\omega} \lesssim 1$, for incident angles $\theta_0 \geqslant \pi/4$. This indicates that the transverse contribution likely scales the same way as the longitudinal contribution to the radiative energy loss in terms of the normal component of the external particle speed, that is, $\propto \cos^2\theta_0$. Thus, one may surmise that the transverse contribution to the radiative energy loss is proportional to $\sin^2(2\theta_0)$ for the incident speeds $\beta \lesssim 0.5$, and it therefore should exhibit a symmetric maximum about $\theta_0 = \pi/4$.

As we have discussed so far, the effect of nonlocality on the energy loss spectra becomes salient for nonretarded speeds. However, relative contribution of the transverse part with respect to the longitudinal part in the energy loss is expected to increase with increasing speed of the external particle, i.e., by going into the regime where the retardation effects dominate. To explore that regime, we show in Fig. 4(a) decomposition into the longitudinal and transverse contributions to the energy loss spectra in a manner similar to that employed in Fig. 3, but for a significantly higher incident speed of $\beta = 0.5$. In this regime, the Ohmic and radiative energy losses attain comparable magnitudes, at least at the frequencies $\overline{\omega} \lesssim 1$ and at the angles of incidence that are not too oblique. Thus, in addition to showing the Ohmic energy loss in Fig. 4(a) and the radiative energy loss in Fig. 4(b), we also show the total energy loss of the external particle in Fig. 4(c), all for various angles of incidence. As expected, no differences are observed between the Drude and Lovat's models in any of the shown spectra, confirming that the nonlocal effects are negligible at such high speed.

The dependencies on the angle of incidence for all contributions shown in Figs. 4(a) and 4(b) at low frequencies are analogous to the trends observed in Fig. 3. As in Fig. 3(a), one notices in Fig. 4(a) that the longitudinal contribution to the Ohmic loss at low frequencies increases with the increasing angle of incidence. This may be tentatively explained by the increasing time that the incident particle spends interacting with the near fields induced by the graphene's charge carriers, which scales as $\propto \sec\theta_0$. However, it is remarkable that, for incident angles $\theta_0 > 60^\circ$, the longitudinal contribution to the Ohmic energy loss at low frequencies in Fig. 4(a) has a comparable magnitude as the same contribution in Fig. 3(a), which is quite surprising given the large difference in the

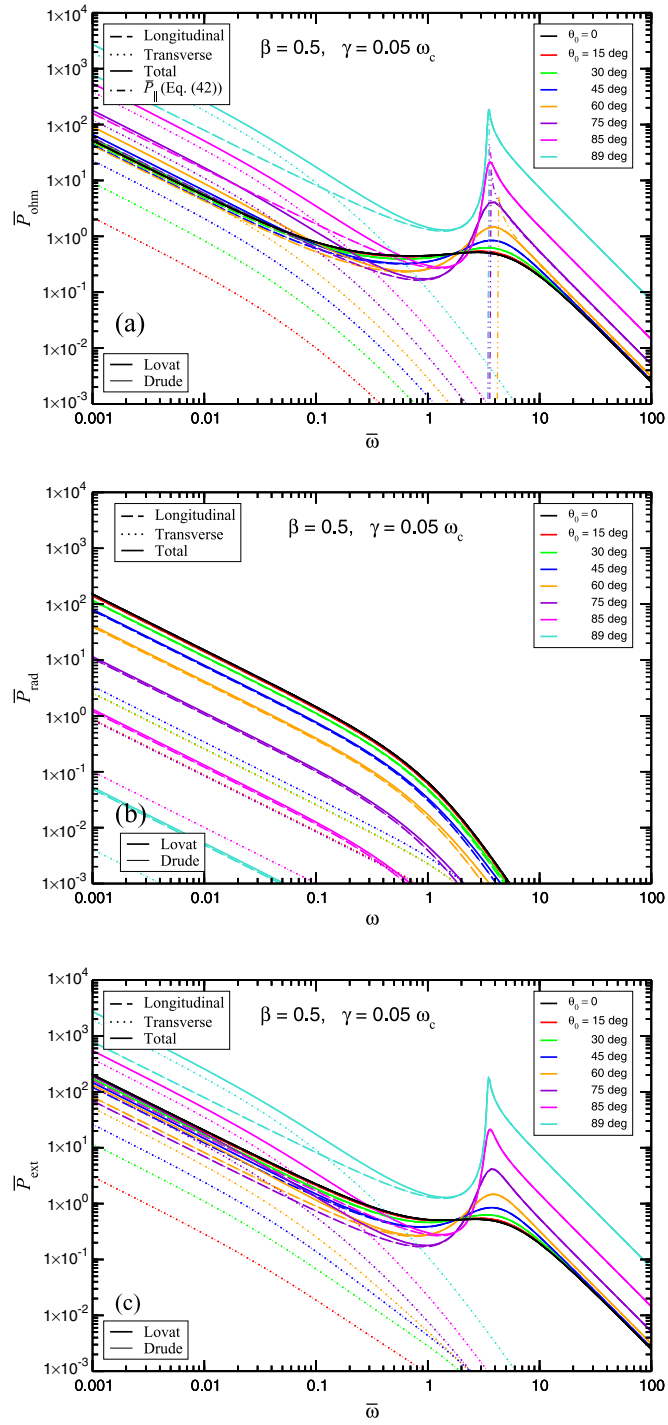

FIG. 4. Normalized integrated probability densities for (a) Ohmic energy loss $\overline{P}_{\rm Ohm}(\overline{\omega})$, (b) radiative energy loss $\overline{P}_{\rm rad}(\overline{\omega})$, and (c) external energy loss $\overline{P}_{\rm ext}(\overline{\omega}) = \overline{P}_{\rm Ohm}(\overline{\omega}) + \overline{P}_{\rm rad}(\overline{\omega})$ for the charged particle speed of $\beta = 0.5$ and for several angles of incidence. The differences between the Lovat's (thick lines) and Drude (thin lines) models, as well as the decomposition of the longitudinal (dashed lines) and transverse (dotted lines) contributions to those integrated densities are shown. Also included are, in (a), calculations for the Ohmic energy loss density at high frequencies using the approximation for $\overline{P}_{||}$ given in Eq. (42) for $\theta_0 \gtrsim 60^\circ$ (dashed–double-dotted curves). The reduced damping rate is fixed at $\overline{\gamma} = 0.05$.

incident speed β between the two figures and the trend observed in Fig. 2.

One can observe in Fig. 4(a) that, while both contributions to the Ohmic loss increase in magnitude with increasing angle of incidence, the longitudinal contribution dominates at higher frequencies, where it exhibits an LDPP-induced peak, whereas the transverse contribution may become dominant at lower frequencies, say $\overline{\omega} \lesssim 0.1$, for sufficiently oblique trajectories, say $\theta_0 \gtrsim 60^\circ$. The latter observation may be rationalized by recalling that the transverse contribution is mostly a result of retardation effects, which are enhanced at lower frequencies and for larger parallel components of the incident speed. At the same time, one observes in Fig. 4(b) that the total radiative energy loss decreases with increasing angle of incidence, with a similar rationale as that provided in the case studied in Fig. 3. Moreover, for all directions of incidence, the transverse contribution to the radiative energy loss is seen to be negligible compared to the longitudinal contribution, while still exhibiting a symmetric maximum at the incident angle $\theta_0 = \pi/4$, as discussed in Fig. 3(b).

The LDPP-induced peak in the longitudinal contribution to the Ohmic energy loss density is observed in Figs. 4(a) and 4(c) at a frequency that is significantly lower than the peak in Fig. 3(a), which is consistent with the trend observed Fig. 2 for increasing total speed β. It is important to notice that this peak grows larger in magnitude for trajectories closer to the parallel direction. This may be also rationalized by noticing that the more time the incident particle spends interacting with the near fields induced by the graphene's charge carriers, the more of its energy will go to the excitation of the LDPP mode in graphene.

It is worthwhile exploring the evolution of the position and the shape of the LDPP-induced peak as the incident angle θ_0 of the charged particle increases towards parallel trajectory. To that effect, we consider the overlap of the resonance condition for exciting the LDPP mode with a dispersion relation [29] $\overline{\omega} = \overline{\omega}_{\rm LDPP}(\overline{k})$, where $\overline{\omega}_{\rm LDPP}(\overline{k}) = \sqrt{2(-1+\sqrt{1+\overline{k}^2})}$ [29], and the so-called kinematic condition $\omega = \mathbf{k}\cdot\mathbf{v}_\parallel$, which maximizes the amplitude A of the excitation mechanism, given in Eq. (7) [32]. One notices that the latter condition covers the region $0 \leqslant \overline{\omega} \leqslant \overline{k}\beta_\parallel$ in the $(\overline{k}, \overline{\omega})$ plane, with an upper boundary that increases with increasing incident angle. In the limit of a (near-) parallel trajectory, we may refer to the longitudinal contribution in Eq. (21) of Ref. [32], to further observe that the Ohmic energy loss *rate* $\mathcal{R} = \frac{dW}{dt}$ is maximized when $\omega = kv_\parallel$ or $\overline{\omega} = \overline{k}\beta_\parallel$. Hence, using the crossing of the LDPP dispersion relation with the upper boundary of the kinematic region in the $(\overline{k}, \overline{\omega})$ plane, we obtain an equation $\overline{\omega}_{\rm LDPP}(\overline{k}) = \overline{k}\beta_\parallel$, which is readily solved for $\overline{k}$ to yield a reduced frequency $\overline{\omega}_\parallel = 2\sqrt{\beta_\parallel^{-2}-1} = 2\sqrt{\beta^{-2}\mathrm{cosec}^2\theta_0 - 1}$, corresponding to a maximal rate of excitation of the LDPP mode for a given incident trajectory. This frequency is found to closely match the positions of the cusplike peaks observed in Fig. 4(a) in the solid curves describing the longitudinal contribution to the Ohmic energy loss for sufficiently large angles of incidence.

Moreover, one can estimate the total energy W lost to the excitation of the LDPP mode for a near-parallel trajectory by invoking the result for the energy loss rate $\mathcal{R}(b)$ for the case of a parallel trajectory with the external particle moving at a fixed distance b from graphene, which is given by the first term in Eq. (21) of Ref. [32]. Using the adiabatic approximation [54], one may then write $W = \frac{1}{v_z}\int_{-\infty}^{\infty} db\, \mathcal{R}(b) \equiv \hbar^2 \int_0^\infty d\omega\, \omega P_\parallel(\omega)$, which, in the limit of zero damping, readily yields an estimate for the longitudinal contribution to the Ohmic energy loss density for a sufficiently grazing angle of incidence

$$\overline{P}_\parallel \approx \frac{2\pi}{\beta^2 \sin(2\theta_0)} \frac{\overline{\omega}}{\overline{\omega}^2+4} \frac{\Theta(\overline{\omega}-\overline{\omega}_\parallel)}{\sqrt{\overline{\omega}^2-\overline{\omega}_\parallel^2}}. \tag{42}$$

We note that the result in Eq. (42) closely reproduces solid curves in Fig. 4(a) for frequencies $\overline{\omega} > \overline{\omega}_\parallel$ and for the incident angles $\theta_0 \gtrsim 60^\circ$.

B. Angular distribution of the emitted THz radiation

Since the transverse contribution to the radiative energy loss densities in the Figs. 3(b) and 4(b) was always found to have much smaller magnitude than the longitudinal contribution, it is instructive to further compare those two contributions in the angular distribution of TR at several typical frequencies. In Fig. 5, we show the angular distribution of the spectral density for TR in reduced units $\overline{\mathcal{S}}(\theta, \phi, \overline{\omega}) = \mathcal{S}/\mathcal{S}_c$ with $\mathcal{S}_c = (Ze)^2/c$ for the external particle with the speed $\beta = 0.5$ and the angle of incidence of $\theta_0 = 60^\circ$, and for three different frequencies $\overline{\omega} = 0.5$, 1, and 5. In the left, middle, and right columns, we show the longitudinal contribution, transverse contribution, and the total angular radiative spectra, respectively [53]. As expected, the radiation patterns are always symmetric with respect to the plane of graphene, as well as with respect to the xz plane, i.e., the plane of incidence of the external charged particle. By the comparison of the left and middle columns, it is seen that, generally, the longitudinal contribution is larger in magnitude when compared to the transverse contribution, but the difference is not as large as implied by the curves in Fig. 4(a). As a matter of fact, by increasing the frequency, the transverse contribution in Fig. 5 becomes even comparable to the longitudinal contribution when viewed in different directions, although both contributions decrease in overall magnitude as the frequency increases.

Another important point to note is that the longitudinal contribution mostly radiates in directions far from the z axis or, more precisely, in directions close to the plane of graphene $\theta \approx \pi/2$, covering a broad range of the polar angle ϕ values with a peak in the (projected) direction of motion of the external particle. At the same time, the transverse contribution mostly radiates in directions close to the z axis, i.e., perpendicular to graphene with θ close to 0 or π, whereas the range of values covered by the polar angle ϕ becomes broader with increasing frequency $\overline{\omega}$, showing a pronounced minimum in the (projected) direction of motion of the external particle $\phi = 0$. Thus, the longitudinal and the transverse contributions to TR exhibit somewhat complementary angular patterns, both with respect to the plane of graphene and the plane of incidence of the external charged particle.

In order to further expose the anisotropy of the radiation patterns, we show in Fig. 6 the cross sections of the angular distribution of the spectral density for TR in the plane of

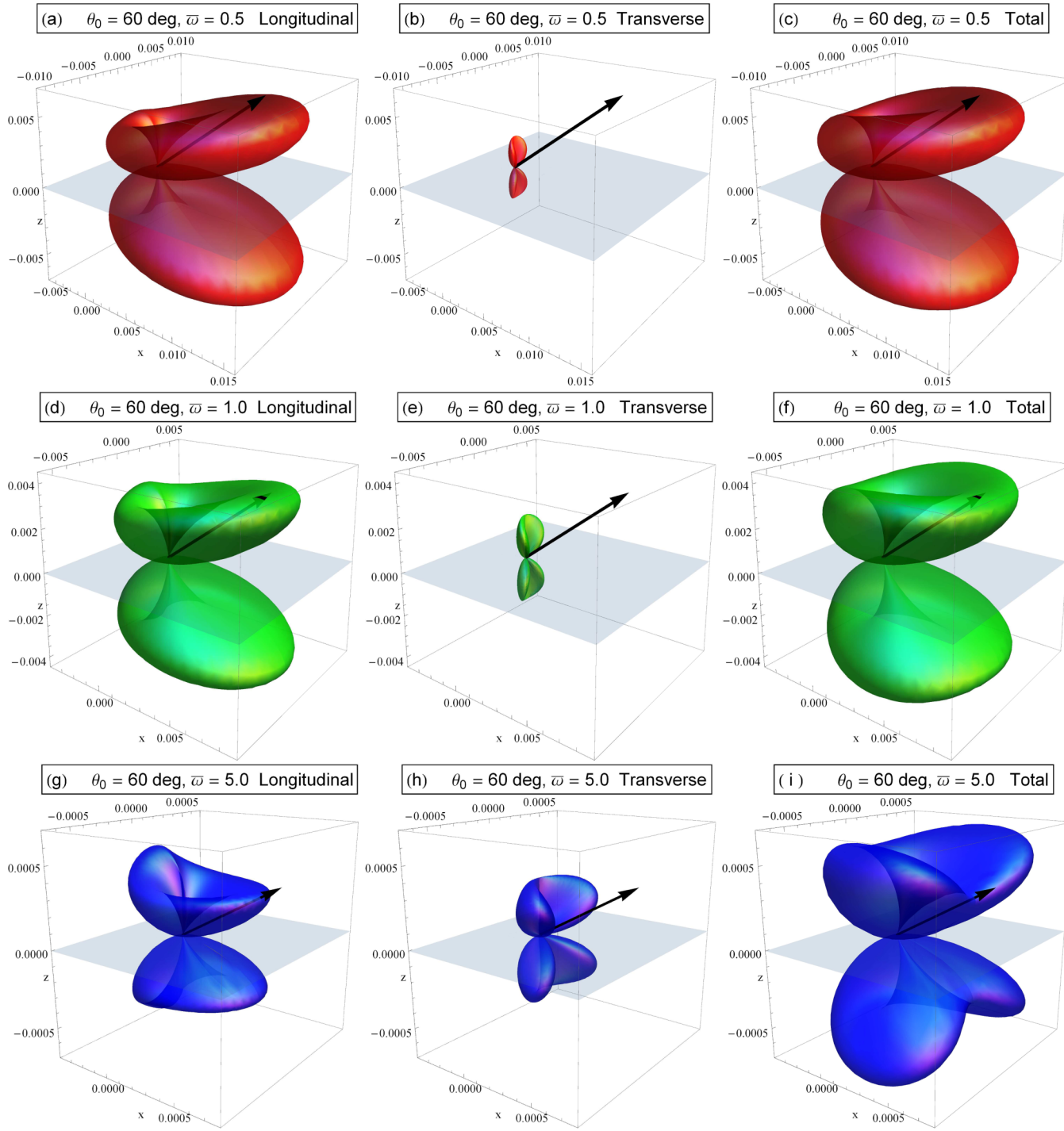

FIG. 5. Angular distribution of the spectral density for TR in reduced units $\overline{\mathcal{S}}(\theta, \phi, \overline{\omega}) = \mathcal{S}/\mathcal{S}_c$ with $\mathcal{S}_c = (Ze)^2/c$ for the external particle with the speed $\beta = 0.5$ and the angle of incidence of $\theta_0 = 60^\circ$, and for three different frequencies $\overline{\omega} = 0.5$, 1, and 5. In the left, middle, and right columns, we show the longitudinal contribution, transverse contribution, and the total angular radiative spectra, respectively. The reduced damping rate is fixed at $\overline{\gamma} = 0.05$ and the Lovat's model has been used for the conductivity tensor.

incidence $\overline{\mathcal{S}}(\theta, \phi = 0, \overline{\omega})$ for an external particle with the speed $\beta = 0.5$ and three angles of incidence, $\theta_0 = 15^\circ$ in Fig. 6(a), $\theta_0 = 45^\circ$ in Fig. 6(b), and $\theta_0 = 85^\circ$ in Fig. 6(c), for several frequencies. These panels represent the total angular distribution, which is identical to the longitudinal contribution, because the factor $\sin^2\phi$ renders the transverse contribution identically zero in the plane of incidence [see Eqs. (16), (23), and (24)]. One can see in Fig. 6 that the overall magnitude of the TR patterns decreases with increasing frequency and with increasing angle of incidence θ_0. In general, all the TR patterns are skewed towards the plane of graphene, and they become more asymmetric with respect to the z axis as the incident trajectory becomes more oblique. Interestingly, while the main lobes of the TR

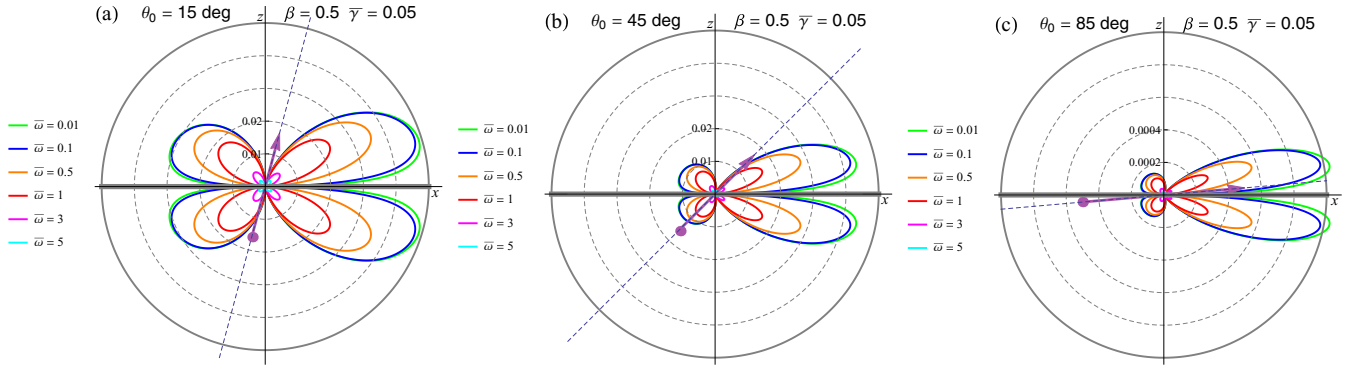

FIG. 6. The cross section of the angular distribution of the spectral density for TR in the plane of incidence $\overline{\mathcal{S}}(\theta, \phi = 0, \overline{\omega})$ for an external particle with the speed $\beta = 0.5$ and three angles of incidence (a) $\theta_0 = 15^\circ$, (b) $\theta_0 = 45^\circ$, and (c) $\theta_0 = 85^\circ$ for several frequencies. These panels represent the total angular distribution, which is identical to the longitudinal contribution. The spectra are calculated employing Lovat's conductivity model for graphene where the reduced damping rate is fixed at $\overline{\gamma} = 0.05$.

patterns occur between the direction of motion of the external particle and graphene, i.e., in a range of emission angles $\theta_0 < \theta < \pi/2$ for the incident angles $\theta_0 = 15^\circ$ and 45°, when the angle of incidence is very close to graphene, $\theta_0 = 85^\circ$, the lobes of the maximum TR occur at the emission angles above the direction of motion $\theta > \theta_0$, although quite close to it. With such peculiar features, it would be quite feasible to perform the CL type of measurements of the emitted radiation in STEM [27], which would be able to not only detect the anisotropy in the angular patterns of the emitted radiation from graphene, but also resolve the polarization of the emitted waves coming from the longitudinal and transverse contributions as the TM and TE polarizations, respectively.

On the other hand, the interaction of externally moving charged particles with 2D materials plays an important role in the prospective design of a stable, highly tunable source of THz radiation. In this regard, there have been several recent proposals to use the EM radiation from graphene induced by a fast electron beam, moving either parallel [24,25] or normal to graphene [26]. In all of those proposals, both the doping density in graphene and the speed of the external particle were suggested as possible tuning parameters for such radiation sources, while the issue of the polarizability of the radiated EM waves was not explicitly addressed. We have seen that the direction of the trajectory of motion of the external particle relative to a 2D material may also be used as a suitable tuning parameter for such sources of radiation, which could possibly help select different polarizations of the radiated EM waves.

C. A search for the transverse mode

While all the above results were obtained using the Drude and the Lovat's models of graphene's conductivity, which cover the frequencies $\overline{\omega} \lesssim 100$, we next investigate the possibility to excite the transverse mode by adopting the optical model of graphene's conductivity, which supports both the LDPP mode due to the intraband electronic excitations at low frequencies and the transverse mode due to the interband electronic transitions involving the range of frequencies $228 < \overline{\omega} < 274$, as discussed in the previous section. Figure 7 depicts the integrated probability density for the Ohmic energy loss $P_{\rm Ohm}$ of a graphene sheet described by the optical conductivity model, along with its decomposition into the longitudinal and transverse contributions, for a charged particle at the speed $\beta = 0.5$. While in Fig. 7(a) we show the results for different angles of incidence, in fig. 7(b) we explore the effects of varying the damping rate $\overline{\gamma}$.

One observes in Fig. 7(a) that the Ohmic energy loss increases in magnitude as the external particle's trajectory becomes more inclined towards graphene, as noted above. Particularly, the LDPP-induced peak at $\overline{\omega} > 1$ in the longitudinal contribution becomes more pronounced with increasing θ_0, whereas at low frequencies, both the longitudinal and transverse contributions to the Ohmic energy loss echo the behavior observed in Fig. 4(a) at $\overline{\omega} < 1$. As was discussed in our previous work [29,31], the very-low-frequency range $\overline{\omega} \lesssim 1$ is where the effect of damping rate is rather strong, and the middle frequency range $1 \lesssim \overline{\omega} \lesssim 100$ is where the excitation of the LDPP mode is dominant, whereas the MIR frequency range of $228 \leqslant \overline{\omega} \leqslant 274$, shown in the insets in Fig. 7, is where the excitation of the transverse mode should take place. In the inset of Fig. 7(a), we see negligibly small energy loss densities for both the longitudinal and transverse contributions, which do increase with the increasing angle of incidence. However, the transverse contribution is always smaller than the longitudinal contribution, which exhibits a high-frequency tail, with a dip that extends over the frequency range $228 < \overline{\omega} < 274$, owing to the finite value of damping rate $\overline{\gamma} = 0.05$, used in Fig. 7(a).

In order to demonstrate a regime where only the transverse contribution would survive, we explore the effects of varying the damping ratio in Fig. 7(b) with a special role played by the idealized case of zero damping $\overline{\gamma} = 0$. Namely, in that case the only mechanism for energy loss of the external charged particle involves Ohmic losses due to excitation of the collective modes in graphene [31]. Specifically, by using Eq. (25) in (28) to evaluate the Ohmic energy loss density by means of Eqs. (37) and (38), we expect that the LDPP mode will give a nonzero longitudinal contribution in the range of frequencies $0 < \overline{\omega} < 228$, and a nonzero transverse contribution in the range of frequencies $228 < \overline{\omega} < 274$, respectively.

While both the longitudinal and transverse contributions to the Ohmic energy loss in Fig. 7(b) show great variability with increasing $\overline{\gamma}$ at low frequencies $\overline{\omega} \lesssim 1$, the situation in the

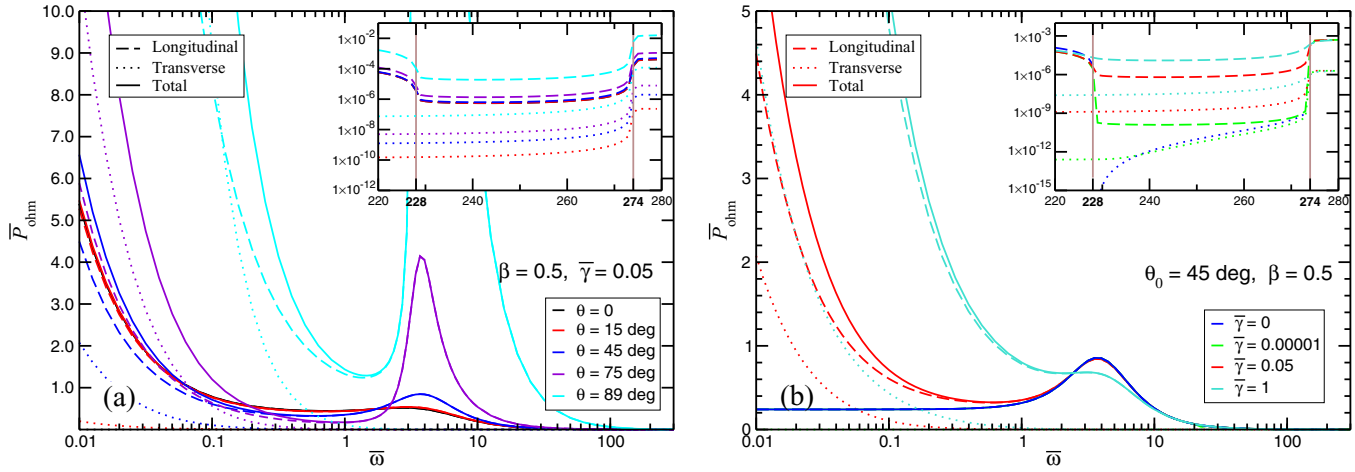

FIG. 7. Integrated probability density for the Ohmic energy loss $P_{\rm Ohm}$ of a graphene sheet described by the optical conductivity model, along with its decomposition into the longitudinal (dashed lines) and transverse (dotted lines) contributions, for a charged particle at the speed $\beta = 0.5$. (a) Represents the results for different angles of incidence with fixed $\overline{\gamma} = 0.05$ and (b) shows the investigation of the effects of varying the damping rate $\overline{\gamma}$ which includes the probability density for the excitations of the LDPP and TDPP modes. The inset of each panel depicts a closer focus at the range of $228 \lesssim \overline{\omega} \lesssim 274$ where the excitation of the transverse mode occurs.

inset to Fig. 7(b) is not much changed compared to the inset to Fig. 7(a), except in the case $\overline{\gamma} = 0$. Namely, one observes in the inset to Fig. 7(b) that, for $\overline{\gamma} = 0$, the tail of the density for the longitudinal contribution (blue dashed line) terminates at the frequency $\overline{\omega} = 228$, whereas the density of the transverse contribution (blue dotted line) shows an onset on that frequency, and it continues increasing with the frequency going up to $\overline{\omega} = 274$, where this contribution terminates. Hence, this shows that the transverse mode may indeed be excited by an external charged particle under oblique incidence upon graphene, although its signature in the energy loss density would not be in the form of a well-defined peak, as in the case of the LDPP mode. Rather, the transverse mode in a graphene with negligible damping of its charge carriers would show as a cusp in the Ohmic energy density at a frequency $\overline{\omega} \leqslant 274$, with a hopelessly low probability.

It should be finally mentioned that the effects of finite temperature make the transverse mode unstable, as shown in Ref. [55]

D. EELS of graphene at high frequencies

While most experiments using EELS of graphene in STEM [18,19,39], as well as the theoretical models of those experiments [39,41,48,51], considered fast electrons under normal incidence upon graphene, there has been recent work that also studied oblique incidence in a momentum-resolved measurement of the dispersion properties of the π and $\sigma + \pi$ "plasmon" peaks in the energy loss spectra [40]. With the advent of the novel monochromatic techniques in STEM [21], it became possible to probe electron energy losses well below 1 eV, thereby accessing the range of the low-energy interband $\pi \to \pi^*$ electronic transitions in intrinsic (undoped) graphene in the Dirac cone approximation. Therefore, we use the eHD model of graphene's conductivity to assess the relative roles of the longitudinal and transverse contributions to both the Ohmic and radiative energy loss spectra of electrons traversing the graphene layer under oblique incidence in a STEM setting.

In Fig. 8(a) we show the integrated probability density of the energy loss $P_{\rm ext}(\omega)$, as a function of the energy ω (we set here $\hbar = 1$), lost by an incident electron with the speed $\beta = 0.5$ for a broad range of incident angles, whereas in the inset to that figure we show the corresponding energy loss due to the emitted TR, $P_{\rm rad}(\omega)$. One notices that the magnitude of the radiation energy loss is very much smaller than $P_{\rm ext}(\omega)$, so that practically $P_{\rm ext}(\omega) \approx P_{\rm Ohm}(\omega)$. One may confirm from Fig. 8(a) that, while the Ohmic energy loss density increases in magnitude with increasing angle of incidence, in a proportion that scales with $\sec\theta_0$ for angles $\theta_0 \gtrsim 60^\circ$, the opposite trend is seen for the radiative energy loss density in the inset to that figure, which decreases with the increasing θ_0. Those trends are consistent with observations made in Figs. 3 and 4 at the THz range of frequencies. Namely, the increase in the Ohmic energy loss scales with increased time the external particle spends interacting with the near fields induced by the excitation of graphene's charge carriers, whereas the decrease in the radiative energy loss is governed by a decrease in the perpendicular component of the external particle speed $\beta\cos\theta_0$, which reduces the "abruptness" of the graphene interaction with the external particle. On the other hand, one notices a small red-shift in the main peaks in $P_{\rm rad}(\omega)$ in comparison to the peak positions in $P_{\rm ext}(\omega)$, but it is interesting that the positions and the shapes of the peaks in each of those densities are rather insensitive to variations of the incident angle. We note that the strong increase observed in both $P_{\rm ext}$ and $P_{\rm rad}$ as $\omega \to 0$ is a signature of the Dirac-term contribution to the eHD conductivity, coming from the low-energy interband $\pi \to \pi^*$ electronic transitions in undoped graphene. Such feature in the experimental EELS data of graphene may have been observed in recent measurements [19,21].

In Fig. 8(b) we show the integrated probability density of the energy loss of the external particle $P_{\rm ext}$ as well as the longitudinal and transverse contributions to that density for several incident angles. One notices that, while the transverse

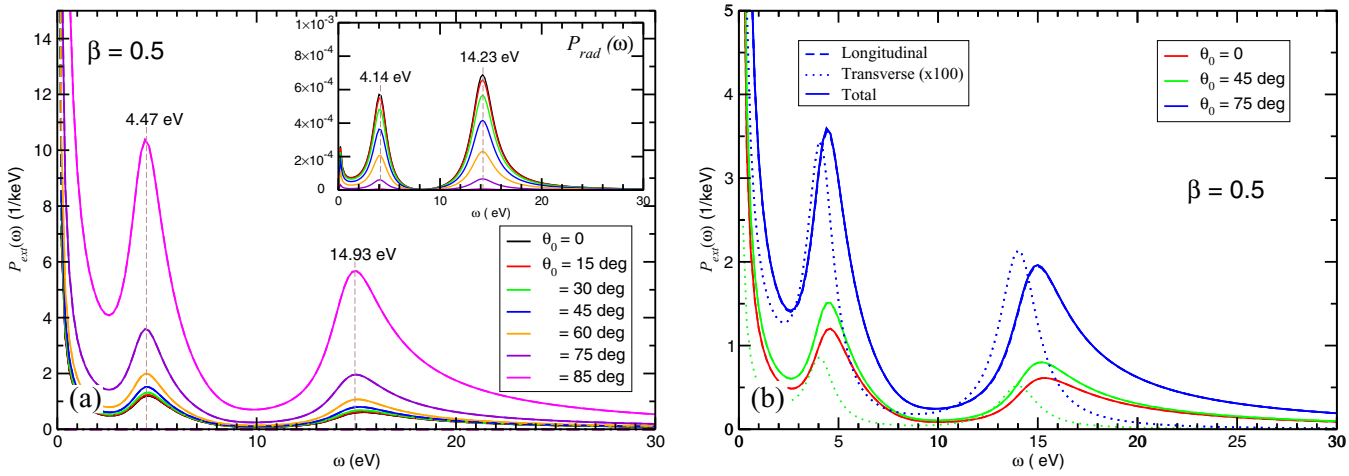

FIG. 8. (a) Integrated probability density of the external energy loss $P_{\rm ext}(\omega)$ as a function of the energy ω (with $\hbar = 1$) lost by an incident electron with the speed $\beta = 0.5$ for a broad range of incident angles. Shown in the inset of (a) is the corresponding energy loss due to the emitted TR, $P_{\rm rad}(\omega)$. Since the magnitude of the radiation energy loss is very much smaller than $P_{\rm ext}(\omega)$, practically $P_{\rm ext}(\omega) \approx P_{\rm Ohm}(\omega)$. (b) Integrated probability density of the energy loss of the external particle $P_{\rm ext}$ (solid lines) as well as the longitudinal (dashed lines) and transverse (dotted lines) contributions to that density for several incident angles. For both panels, the eHD conductivity model for graphene, with the parameters fixed at $n_\pi^0 = 38\ {\rm nm}^{-2}$, $n_\sigma^0 = 115\ {\rm nm}^{-2}$, $\omega_{\pi r} = 4.19$ eV, $\omega_{\sigma r} = 14.15$ eV, $\gamma_\pi = 2.04$ eV, $\gamma_\sigma = 2.178$ eV, and $\omega_* = 3.54$ eV, is used.

contribution is absent for the normal incidence, its density for oblique incidence resembles that of the longitudinal contribution, except for a small red-shift in the main peak positions and a significantly smaller magnitude. While the data for $P_{\rm ext}(\omega)$ in Fig. 8(b) practically refer to the Ohmic energy loss, we show in Fig. 9 a decomposition of both the Ohmic [Fig. 9(a)] and the radiative [Fig. 9(b)] energy losses into their respective longitudinal and transverse contributions for the incident angle $\theta_0 = 45^\circ$. What is remarkable to observe in Fig. 9(b) is that the transverse and longitudinal contributions to the radiative energy loss have similar magnitudes, which is not the case for such contributions to the Ohmic energy loss shown in Figs. 8(b) and 9(a). Moreover, unlike the red-shifts observed among the peak positions in the longitudinal and transverse contributions to the Ohmic energy loss in Figs. 8(b) and 9(a), one sees in Fig. 9(b) that the longitudinal and transverse contributions to the radiative energy loss exhibit main peaks at approximately equal energies.

Finally, in Fig. 10, we show the joint probability densities for the longitudinal (left column) and transverse (middle column) contributions to the Ohmic energy loss, along with their sum, $F_{\rm Ohm}(k, \phi, \omega)$ (right column), which practically represents the total energy loss density of the external charged particle, given the smallness of the radiative energy loss. Results show the dependence on the wave number k and the energy loss ω, in the direction of $\phi = \pi/4$ with respect to the x axis, i.e., the (projected) direction of motion for an external particle having the speed $\beta = 0.5$ and taking three angles of incidence relative to the z axis: $\theta_0 = 0$ (top row), $\theta_0 = 45^\circ$ (middle row), and $\theta_0 = 75^\circ$ (bottom row). One notices that, for $\theta_0 = 45^\circ$, there is only a moderate increase in the longitudinal contribution compared to the normal incidence $\theta_0 = 0$, accompanied by a small transverse contribution near $k = 0$ and $\omega = 0$. By increasing the angle of incidence to $\theta_0 = 75^\circ$, there is a substantial increase in the longitudinal contribution for intermediate wave numbers $k \sim k_{\rm max}$, at the energies intermediate between the two main peaks corresponding to the π and $\sigma + \pi$ "plasmons," as well as an increase in that contribution for large wave numbers $k \gtrsim 2k_{\rm max}$ at the energy close to that of the $\sigma + \pi$ "plasmon."

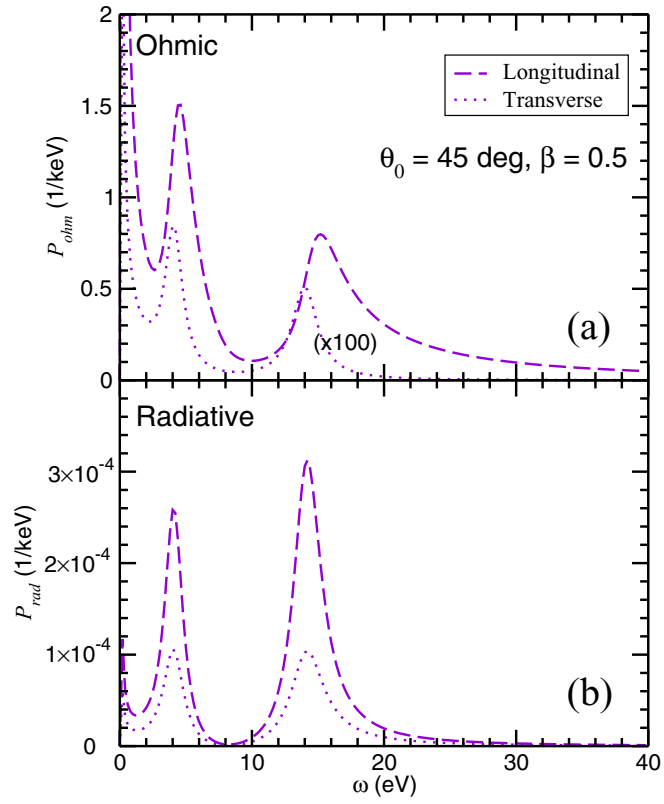

FIG. 9. A decomposition of (a) the Ohmic and (b) the radiative energy losses into their respective longitudinal (dashed lines) and transverse (dotted lines) contributions for the incident angle $\theta_0 = 45^\circ$. For both panels, the eHD conductivity model for graphene, with the parameters fixed at $n_\pi^0 = 38\ {\rm nm}^{-2}$, $n_\sigma^0 = 115\ {\rm nm}^{-2}$, $\omega_{\pi r} = 4.19$ eV, $\omega_{\sigma r} = 14.15$ eV, $\gamma_\pi = 2.04$ eV, $\gamma_\sigma = 2.178$ eV, and $\omega_* = 3.54$ eV, is used.

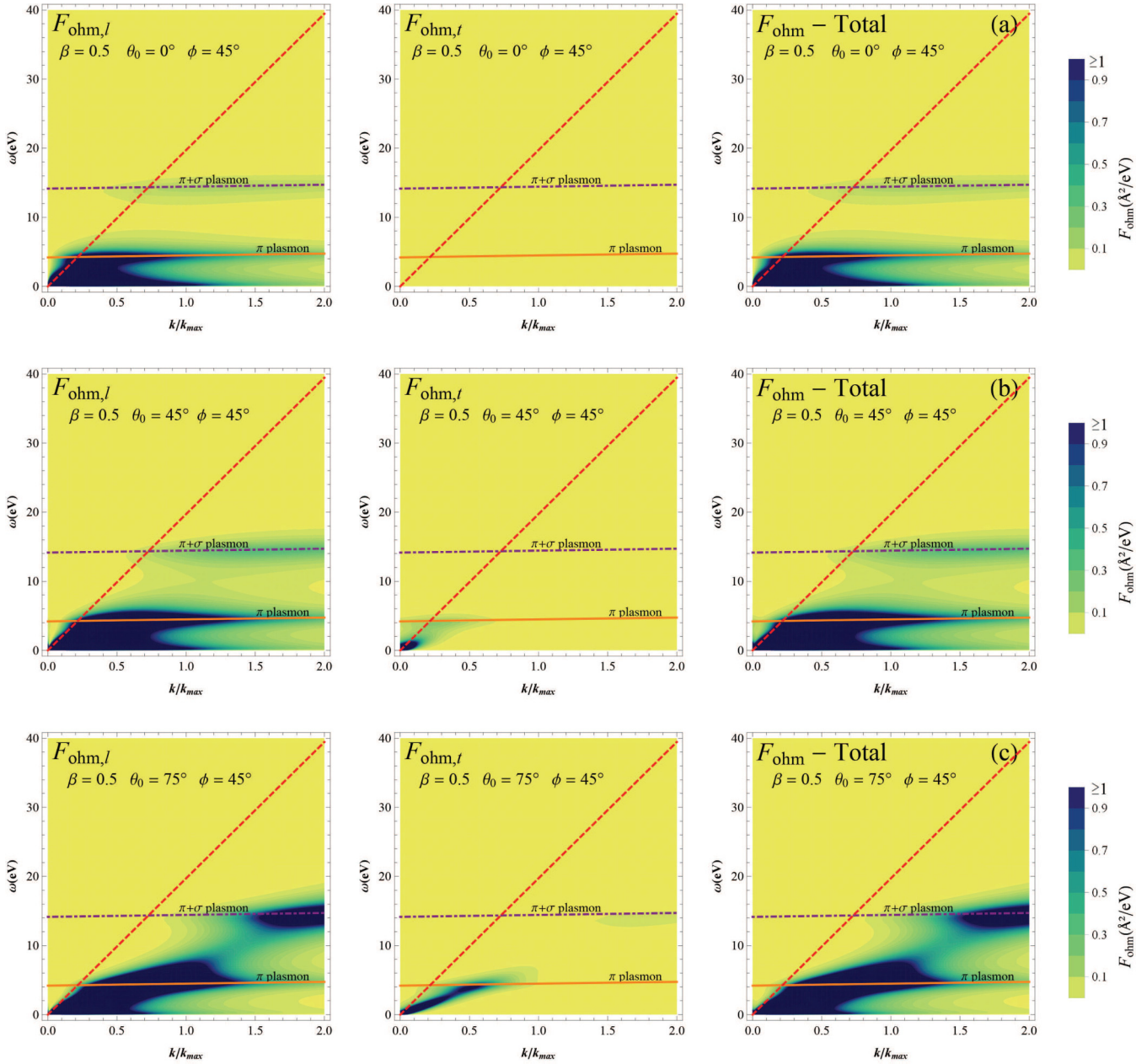

FIG. 10. Joint probability densities for the longitudinal (left column) and transverse (middle column) contributions to the Ohmic energy loss, along with their sum $F_{\rm Ohm}(k,\phi,\omega)$ (right column), which practically represents the total energy loss density of the external charged particle, given the smallness of the radiative energy loss. Results are shown as functions of the wave number k and the energy loss ω, in the direction of $\phi = \pi/4$ with respect to the x axis, i.e., the (projected) direction of motion for an external particle having the speed $\beta = 0.5$ and for three angles of incidence relative to the z axis: $\theta_0 = 0$ (top row), $\theta_0 = 45^\circ$ (middle row), and $\theta_0 = 75^\circ$ (bottom row). For all panels, the eHD conductivity model for graphene, with the parameters fixed at $n_\pi^0 = 38\ \text{nm}^{-2}$, $n_\sigma^0 = 115\ \text{nm}^{-2}$, $\omega_{\pi r} = 4.19$ eV, $\omega_{\sigma r} = 14.15$ eV, $\gamma_\pi = 2.04$ eV, $\gamma_\sigma = 2.178$ eV, and $\omega_* = 3.54$ eV, is used. Also shown are the nonrelativistic dispersion relations of the π (solid orange line) and $\pi+\sigma$ (dash-dotted purple line) plasmons for single-layer graphene [51], and the light line by the dashed red line. Here, $k_{\rm max} = 0.1\ \text{nm}^{-1}$.

We note that the color coding in Fig. 10 is adopted so that all the probability density values exceeding the relatively small value of 1 Å^2/eV are shown in dark blue, as indicated in the color bars. This is done so that subdominant resonant features can be observable in that figure, in addition to the dominant peaks.

What is interesting to observe in the middle panel of the bottom row in Fig. 10 is that the transverse contribution exhibits a well-defined modelike intensity for the incident angle $\theta_0 = 75^\circ$, which extends between $\omega = 0$ and the energy of the π "plasmon," with a peculiar linear dispersion with k, lying well below the light line. Noting that the magnitude of the joint probability densities is shown in Fig. 10 with equal scaling factors, this observation is even more remarkable, given that the transverse contribution plays negligible role in the integrated Ohmic energy loss in Figs. 8(b) and 9(a).

Like in the case of the angular distribution of the radiation energy loss in the far-field region at the THz frequencies in Fig. 5, one may assert from Fig. 10 that the momentum- and angle-resolved density of the Ohmic energy loss in graphene at the MIR to UV frequencies also exhibits strong anisotropy and complementarity in its longitudinal and transverse contributions. This points to the potentially interesting effects of the in-plane anisotropy in the excitation of the high-energy interband electronic transitions in graphene by a fast electron under oblique incidence, which could be possibly observed in STEM via EELS by using a detector with narrow slit to collect the transmitted electrons, and by rotating the slit with respect to the incident plane in order to probe angles ϕ that would expose the transverse contribution to the Ohmic energy loss.

IV. CONCLUSIONS

We have studied the interaction of an external charged particle with single-layer graphene in broad ranges of the relative particle speed $\beta = v/c$ and the incidence angle θ_0 with respect to an axis normal to the plane of graphene. We have evaluated and compared decompositions of the Ohmic and radiative energy losses of the external particle into their longitudinal and transverse components in order to emphasize the importance of the oblique incidence for generating electromagnetic (EM) fields with different polarizations by two types of the excitation processes of charge carriers in graphene. Those processes were described by defining two in-plane dielectric functions, which incorporate suitable models of graphene's longitudinal and transverse electrical conductivity. Our observations are given below.

In the THz frequency range, we have used the standard Drude model for conductivity describing the low-energy intraband excitations of Dirac's electrons in graphene, as well as the model due to Lovat *et al.*, which introduces nonlocal effects in the conductivity of graphene at those frequencies. While the Drude model is suitable for describing the longitudinal Dirac plasmon polariton (LDPP) mode in the supra-THz frequency range, it also reveals the effects of retardation, which are most prominent at the sub-THz frequencies. By comparing the results from the Lovat's and Drude models, we have assessed the effects of the nonlocality in the integrated energy loss densities at the THz frequencies. We have found that this effect is only pronounced around the THz frequency for the Ohmic energy loss at very low speeds of the incident particle, i.e., in the nonretarded regime. In that regime, the radiative energy loss is heavily suppressed and it exhibits no effect of the nonlocality, which is expected, since the radiative loss is a purely relativistic phenomenon.

On the other hand, in the retarded regime, i.e., for high incident speeds, the Ohmic and the radiative energy losses can attain comparable magnitudes at the sub-THz frequencies and at the angles of incidence that are not too oblique. Moreover, in this regime, both the longitudinal and transverse contributions to the integrated Ohmic energy loss density increase with increasing angle of incidence. This is true for a full range of frequencies, from the THz to the UV, and it may be tentatively explained by the increasing time that the incident particle spends interacting with the near fields induced by the graphene's charge carriers, which scales as $\propto \sec\theta_0$. The longitudinal contribution to the Ohmic energy loss dominates at the supra-THz frequencies, where it exhibits a pronounced peak related to the LDPP, whereas the transverse contribution is heavily suppressed at such frequencies. On the other hand, at the sub-THz frequencies, the transverse contribution to the Ohmic energy loss may even surpass the longitudinal contribution for high enough speeds and sufficiently oblique trajectories of the charged particle. This may be rationalized by recalling that the transverse contribution is mostly a result of retardation effects, which are enhanced at lower frequencies and for larger parallel components of the incident speed.

The longitudinal contribution to the integrated radiation energy loss density decreases with increasing angle of incidence in a manner that seems to be governed by a decrease in the normal component of the external particle speed $\beta\cos\theta_0$. This is true for a full range of frequencies, from the THz to the UV, and it may be explained by recalling that the radiation is most effectively produced by accelerating the charge carriers in graphene, so that a reduction in the normal component of the speed would bring down the "abruptness" of graphene's interaction with the external charged particle, and hence it would reduce the production of the transition radiation (TR) from graphene. The transverse contribution to the integrated radiation energy loss density exhibits a symmetric maximum at the incident angle $\theta_0 = \pi/4$, and is found to be much smaller than the longitudinal contribution to the integrated radiation energy loss in the full range of frequencies, for all incident speeds and all angles of incidence.

However, this relation between these two contributions to the radiation energy losses is different when considering the angle-resolved spectra of the emitted TR. Namely, both the longitudinal and the transverse contributions to the TR exhibit rather anisotropic angular distributions, with somewhat complementary patterns of the emitted EM field intensity. Specifically, while the longitudinal contribution mostly radiates in broad patterns skewed towards the plane of graphene, the transverse contribution radiates preferably in a direction perpendicular to graphene, but away from the plane of incidence of the external particle. Interestingly, unlike the case of the integrated radiative energy loss density, peaks in the radiation lobes in the angular distribution that result from the longitudinal and transverse contributions may attain comparable magnitudes when viewed in different directions. Therefore, we propose that a CL type of measurements of the emitted radiation in STEM could be used to explore this anisotropy in the angular patterns of the emitted radiation from graphene, where detection of the polarization of the emitted EM waves as the TM or TE may be used to identify contributions coming from the longitudinal or transverse excitation processes in graphene, respectively.

By adding a contribution due to the low-energy interband electron excitations in graphene to the Drude model, we have used an optical conductivity model that is valid up to the MIR range of frequencies in order to explore the possibility of exciting a transverse collective mode in doped graphene by means of a fast electron under oblique incidence. We

have indeed found an evidence that such excitation would be identifiable in the transverse contribution to the integrated Ohmic energy loss in an ideal case of doped graphene with zero damping, but with an impractically low probability. This confirms that, despite the fact that the Joule energy dissipation rate in the transverse dielectric function could be substantial in the sub-THz range, the energy confined in the near field of graphene due to excitation of the transverse mode is negligible in comparison with that of the longitudinal mode, as shown in Ref. [56].

Finally, we have used an extended hydrodynamic model of graphene's conductivity in the MIR to UV frequency range to study EELS for electrons traversing the graphene layer under oblique incidence in a STEM setting. We have found that the integrated radiation energy loss density is much smaller than the integrated Ohmic energy loss density, and that they both exhibit main peak features with the positions and shapes that are insensitive to the variation in the incident angle. Moreover, while the transverse contribution is much smaller than the longitudinal contribution in the integrated Ohmic energy loss, the longitudinal and transverse contributions in the integrated radiative energy loss have comparable magnitudes but, even when added together, they constitute a negligible fraction of the total integrated energy loss of the external charged particle. As for the dependence on the angle of incidence, observations in the MIR to UV range are analogous to those at the THz frequencies: the overall magnitude of the integrated Ohmic energy loss density increases and the integrated radiative energy loss density decreases with increasing angle of incidence.

Considering the momentum k and the angle ϕ dependence of a joint probability density for the Ohmic energy loss in graphene, we have observed an increase in the longitudinal contribution in different regions of the (k, ϕ) plane with increasing angle of incidence θ_0 of the external charge particle. For a sufficiently oblique incident trajectory, we have also observed a well-defined, modelike feature in the transverse contribution to the Ohmic energy loss, exhibiting a linear energy dispersion in the direction $\phi = \pi/4$ with respect to the incident plane of the charged particle. We therefore propose an experiment in STEM using a narrow slit detector to collect obliquely incident electrons upon graphene, which can be rotated with respect to the plane of incidence in order to search for such directional modes as a signature of the transverse excitation processes in graphene at the MIR to the UV range of frequencies.

ACKNOWLEDGMENTS

S.S., J.L.G., and N.R.A. acknowledge the financial support from CONICET (Grants No. PIP 11220120100374 and No. PIP 11220170100353) from Argentina. Z.L.M. acknowledges support from the Natural Sciences and Engineering Research Council of Canada (Grant No. 2016-03689).

[1] A. Nemilentsau, T. Low, and G. Hanson, Phys. Rev. Lett. **116**, 066804 (2016).
[2] K. F. Mak and J. Shan, Nat. Photonics **10**, 216 (2016).
[3] A. Krasnok, S. Lepeshov, and A. Alú, Opt. Express **26**, 15972 (2018).
[4] C. Hogan, O. Pulci, P. Gori, F. Bechstedt, D. S. Martin, E. E. Barritt, A. Curcella, G. Prevot, and Y. Borensztein, Phys. Rev. B **97**, 195407 (2018).
[5] A. H. Castro Neto, F. Guinea, N. M. R. Peres, K. S. Novoselov, and A. K. Geim, Rev. Mod. Phys. **81**, 109 (2009).
[6] M. Jablan, M. Soljačić, and H. Buljan, Proc. IEEE **101**, 1689 (2013).
[7] A. C. Ferrari, F. Bonaccorso, V. Falko, K. S. Novoselov, S. Roche, P. Boggild, S. Borini, F. H. L. Koppens, V. Palermo, N. Pugno, J. A. Garrido, R. Sordan, A. Bianco, L. Ballerini, M. Prato, E. Lidorikis, J. Kivioja, C. Marinelli, T. Ryhänen, A. Morpurgo *et al.*, Nanoscale **7**, 4598 (2015).
[8] T. Low, P.-Y. Chen, and D. N. Basov, Phys. Rev. B **98**, 041403 (2018).
[9] T. Low and P. Avouris, ACS Nano **8**, 1086 (2014).
[10] L. Wu, J. Guo, H. Xu, X. Dai, and Y. Xiang, Photonics Res. **4**, 262 (2016).
[11] E. Morales-Narvaez, L. Baptista-Pires, A. Zamora-Galvez, and A. Merkoci, Adv. Mater. **29**, 1604905 (2016).
[12] Y. D. Kim, Y. Gao, R.-J. Shiue, L. Wang, O. B. Aslan, M.-H. Bae, H. Kim, D. Seo, H.-J. Choi, S. H. Kim, A. Nemilentsau, T. Low, C. Tan, D. K. Efetov, T. Taniguchi, K. Watanabe, K. L. Shepard, T. F. Heinz, D. Englund, and J. Hone, Nano Lett. **18**, 934 (2018).
[13] A. N. Grigorenko, M. Polini, and K. S. Novoselov, Nat. Photonics **6**, 749 (2012).
[14] F. J. G. de Abajo, ACS Photonics **1**, 135 (2014).
[15] R. F. Egerton, *Electron Energy-Loss Spectroscopy in the Electron Microscope* (Springer, New York, 2011).
[16] C. Colliex, M. Kociak, and O. Stéphan, Ultramicroscopy **162**, A1 (2016).
[17] F. S. Hage, T. P. Hardcastle, A. J. Scott, R. Brydson, and Q. M. Ramasse, Phys. Rev. B **95**, 195411 (2017).
[18] T. Eberlein, U. Bangert, R. R. Nair, R. Jones, M. Gass, A. L. Bleloch, K. S. Novoselov, A. Geim, and P. R. Briddon, Phys. Rev. B **77**, 233406 (2008).
[19] P. Wachsmuth, R. Hambach, M. K. Kinyanjui, M. Guzzo, G. Benner, and U. Kaiser, Phys. Rev. B **88**, 075433 (2013).
[20] M. J. Mohn, R. Hambach, P. Wachsmuth, C. Giorgetti, and U. Kaiser, Phys. Rev. B **97**, 235410 (2018).
[21] J. C. Idrobo and W. Zhou, Ultramicroscopy **180**, 156 (2017).
[22] W. Zhou, J. Lee, J. Nanda, S. T. Pantelides, S. J. Pennycook, and J.-C. Idrobo, Nat. Nanotechnol. **7**, 161 (2012).
[23] J. H. Warner, Y.-C. Lin, K. He, M. Koshino, and K. Suenaga, Nano Lett. **14**, 6155 (2014).
[24] T. Zhan, D. Han, X. Hu, X. Liu, S.-T. Chui, and J. Zi, Phys. Rev. B **89**, 245434 (2014).
[25] S. Liu, C. Zhang, M. Hu, X. Chen, P. Zhang, S. Gong, T. Zhao, and R. Zhong, Appl. Phys. Lett. **104**, 201104 (2014).
[26] K.-C. Zhang, X.-X. Chen, C.-J. Sheng, K. J. A. Ooi, L. K. Ang, and X.-S. Yuan, Opt. Express **25**, 20477 (2017).

[27] E. J. R. Vesseur, J. Aizpurua, T. Coenen, A. Reyes-Coronado, P. E. Batson, and A. Polman, MRS Bull. **37**, 752 (2012).
[28] A. Brandstetter-Kunc, G. Weick, C. A. Downing, D. Weinmann, and R. A. Jalabert, Phys. Rev. B **94**, 205432 (2016).
[29] Z. L. Miskovic, S. Segui, J. L. Gervasoni, and N. R. Arista, Phys. Rev. B **94**, 125414 (2016).
[30] K. Akbari, Z. L. Miskovic, S. Segui, J. L. Gervasoni, and N. R. Arista, ACS Photonics **4**, 1980 (2017).
[31] K. Akbari, Z. L. Miskovic, S. Segui, J. L. Gervasoni, and N. R. Arista, Nanotechnology **29**, 225201 (2018).
[32] Z. L. Miskovic, K. Akbari, S. Segui, J. L. Gervasoni, and N. R. Arista, Nucl. Instrum. Methods Phys. Res., Sect. B **422**, 18 (2018).
[33] J. D. Jackson, *Classical Electrodynamics* (Wiley, New York, 1975).
[34] Y. V. Bludov, A. Ferreira, N. M. R. Peres, and M. I. Vasilevskiy, Int. J. Mod. Phys. B **27**, 1341001 (2013).
[35] K. F. Allison and Z. L. Miskovic, Nanotechnology **21**, 134017 (2010).
[36] V. Despoja, T. Djordjević, L. Karbunar, I. Radović, and Z. L. Miskovic, Phys. Rev. B **96**, 075433 (2017).
[37] J. A. Stratton, I. Antennas, and P. Society, *Electromagnetic Theory*, an IEEE Press classic reissue (Wiley, Hoboken, NJ, 2007).
[38] G. Lovat, G. W. Hanson, R. Araneo, and P. Burghignoli, Phys. Rev. B **87**, 115429 (2013).
[39] F. J. Nelson, J.-C. Idrobo, J. D. Fite, Z. L. Miskovic, S. J. Pennycook, S. T. Pantelides, J. U. Lee, and A. C. Diebold, Nano Lett. **14**, 3827 (2014).
[40] S. C. Liou, C.-S. Shie, C. H. Chen, R. Breitwieser, W. W. Pai, G. Y. Guo, and M.-W. Chu, Phys. Rev. B **91**, 045418 (2015).
[41] T. Djordjević, I. Radović, V. Despoja, K. Lyon, D. Borka, and Z. L. Miskovic, Ultramicroscopy **184**, 134 (2018).
[42] L. A. Falkovsky and S. S. Pershoguba, Phys. Rev. B **76**, 153410 (2007).
[43] F. H. L. Koppens, D. E. Chang, and F. J. G. de Abajo, Nano Lett. **11**, 3370 (2011).
[44] S. Das Sarma, S. Adam, E. H. Hwang, and E. Rossi, Rev. Mod. Phys. **83**, 407 (2011).
[45] B. Wunsch, T. Stauber, F. Sols, and F. Guinea, New J. Phys. **8**, 318 (2006).
[46] S. A. Mikhailov and K. Ziegler, Phys. Rev. Lett. **99**, 016803 (2007).
[47] T. Stauber, J. Phys.: Condens. Matter **26**, 123201 (2014).
[48] V. Despoja, D. Novko, K. Dekanić, M. Šunjić, and L. Marušić, Phys. Rev. B **87**, 075447 (2013).
[49] D. Novko, M. Šunjić, and V. Despoja, Phys. Rev. B **93**, 125413 (2016).
[50] A. G. Marinopoulos, L. Reining, A. Rubio, and V. Olevano, Phys. Rev. B **69**, 245419 (2004).
[51] V. B. Jovanović, I. Radović, D. Borka, and Z. L. Miskovic, Phys. Rev. B **84**, 155416 (2011).
[52] T. Stauber, N. M. R. Peres, and A. K. Geim, Phys. Rev. B **78**, 085432 (2008).
[53] See Supplemental Material at http://link.aps.org/supplemental/10.1103/PhysRevB.98.195410 for additional results.
[54] Y.-H. Song, Y.-N. Wang, and Z. L. Miskovic, Phys. Rev. A **63**, 052902 (2001).
[55] A. Gutiérrez-Rubio, T. Stauber, and F. Guinea, J. Opt. **15**, 114005 (2013).
[56] X. Lin, N. Rivera, J. J. Lopez, I. Kaminer, H. Chen, and M. Soljacic, New J. Phys. **18**, 105007 (2016).